

REPORT DOCUMENTATION PAGE

Public reporting burden for this collection of information is estimated to average 1 hour per response, including the time for reviewing existing data sources, gathering and maintaining the data needed, and completing and reviewing the collection of information. Send comments regarding this burden estimate or any other aspect of this collection of information, including suggestions for reducing this burden to Washington Headquarters Service, Directorate for Information Operations and Reports, Paperwork Reduction Project (0704-0188) Washington DC 20503
PLEASE DO NOT RETURN YOUR FORM TO THE ABOVE ADDRESS.

1. REPORT DATE (DD-MM-YYYY) 11-20-2007		2. REPORT DATE Final Report		3. DATES COVERED: (From - To) 4/1/2004 - 7/31/2007	
4. TITLE AND SUBTITLE NUMERICAL COMPUTATION IN MAGNETO-FLUID DYNAMICS				5a. CONTRACT NUMBER	
				5b. GRANT NUMBER FA9550-04-1-0155	
				5c. PROGRAM ELEMENT NUMBER	
6. AUTHOR(S) Robert W. MacCormack				5d. PROJECT NUMBER	
				5e. TASK NUMBER	
				5f. WORK UNIT NUMBER	
7. PERFORMING ORGANIZATION NAME(S) AND ADDRESS(ES) Stanford University 651 Serra Street Stanford, CA 94305				8. PERFORMING ORGANIZATION REPORT NUMBER TAAAX	
9. SPONSORING/MONITORING AGENCY NAME(S) AND ADDRESS(ES) Air Force Office of Scientific Research 875 North Randolph Street Arlington, VA 22203-1768				10. SPONSOR/MONITOR'S ACRONYM(S) AFOSR	
				AGENCY REPORT NUMBER	
12. DISTRIBUTION AVAILABILITY STATEMENT unlimited Approved for public release. Distribution is unlimited					
13. SUPPLEMENTARY NOTES					
14. ABSTRACT Magneto-Hydro-Dynamics (MHD) or more generally Magneto-Fluid-Dynamics (MFD) offers a potential breakthrough in both hypersonic vehicle design and propulsion. Reductions in both drag and heat transfer and flow control using magnetic fields can be important for enabling a hypersonic vehicle to pass more efficiently and safely through the atmosphere. Magnetic and electric fields placed within the propulsion system may enable the extraction of electrical energy from the ionized flow entering the engine, thus slowing the air speed without the usual large losses in total pressure caused by conventional shock wave deceleration and thereby enhancing complete combustion, and then later returning the extracted energy back into the flow after combustion for further acceleration. These potential benefits may or may not be realizable for air vehicle design. Realistic aerodynamic simulations, under the conditions of expected low electrical conductivities and strong magnetic fields, will be required. The solution of the complete equations governing magneto-fluid dynamics, including magnetic induction and diffusion, within strong magnetic fields can introduce severe numerical simulation difficulties. The goal of this research is to develop algorithms for their solution.					
15. SUBJECT TERMS Magneto-Hydro-Dynamics, strong magnetic fields, ionized flow, aerodynamic simulations, algorithm development					
16. SECURITY CLASSIFICATION OF:			17. LIMITATION OF ABSTRACT UU	18. NUMBER OF PAGES 6	19a. NAME OF RESPONSIBLE PERSON Robert W. MacCormack
a. REPORT U	b. ABSTRACT U	c. THIS PAGE U			20b. TELEPHONE NUMBER (include area code) 650-723-4627

FINAL REPORT

MAGNETO-FLUID DYNAMICS CALCULATIONS FOR AERODYNAMICS

AFOSR GRANT FA9550-04-1-0155

Robert W. MacCormack
Department of Aeronautics and Astronautics
Stanford University

Abstract

Magneto-Hydro-Dynamics (MHD) or more generally Magneto-Fluid-Dynamics (MFD) offers a potential breakthrough in both hypersonic vehicle design and propulsion. Reductions in heat transfer and flow control using magnetic fields can be important for enabling a hypersonic vehicle to pass more efficiently and safely through the atmosphere. Magnetic and electric fields placed within the propulsion system may enable the extraction of electrical energy from the ionized flow entering the engine, while simultaneously slowing the fluid, without losses in total pressure caused by shockwaves, and enhancing complete fuel combustion. The extracted energy can be returned back into the flow after combustion for further flow acceleration and engine thrust. These potential benefits may or may not be realizable. Realistic aerodynamic simulations, under the conditions of expected low electrical conductivities and strong magnetic fields, will be required. The solution of the complete equations governing magneto-fluid dynamics, including magnetic induction and diffusion within strong magnetic fields, are needed to perform the required flow simulations. The MFD equations can introduce severe numerical simulation difficulties. The goal of this research is to develop algorithms for their solution for weakly ionized aerodynamic flows for both internal and external MFD flows.

The algorithms presented herein contain numerical procedures for solving the governing MFD equations, applying boundary conditions, evaluating temperature and pressures for an open ended set of fluid species composing the flow, and determining the electrical conductivity of the ionized gas. Applications relevant to flows past flight vehicles and through scram jet engines are presented.

I. Background

There are several descriptions of MFD flows, each with their own assumptions and set of governing equations. The full set of MFD equations and a simplified set, called the "Low Magnetic Reynolds Number Approximation equations, are presented below. The latter set is prevalent today. This is because of its simplicity and belief that it sufficiently describes aerodynamic flows within electromagnetic fields. However, an example is also presented showing that this may not be true. The research of this contract was aimed toward the development of algorithms for the full set of MFD equations.

The Equations of Magneto-Fluid Dynamics

1) The Navier-Stokes equations $\frac{\partial U}{\partial t} + \frac{\partial F}{\partial x} + \frac{\partial G}{\partial y} + \frac{\partial H}{\partial z} = 0$, with $U = [\rho, \rho u, \rho v, \rho w, e]^T$,

20071228021

density ρ , velocities u, v and w , total energy per unit volume e .

2) Maxwell's equations - The Ampere-Maxwell equation $\frac{\partial \vec{E}}{\partial t} = \frac{1}{\epsilon_e} \left(\frac{\vec{\nabla} \times \vec{B}}{\mu_e} - \vec{J} \right)$

Faraday's equation $\frac{\partial \vec{B}}{\partial t} = -\vec{\nabla} \times \vec{E}$

with constraints $\vec{\nabla} \cdot \vec{E} = \frac{1}{\epsilon_e} \rho^c$ and $\vec{\nabla} \cdot \vec{B} = 0$,

with electric field \vec{E} , magnetic field \vec{B} , current density \vec{J} , inductive capacity ϵ_e ,

magnetic permeability $\mu_e = 4\pi \times 10^{-7} \frac{kg \cdot m}{(coulomb)^2}$ and charge density ρ^c .

3) Generalized Ohm's law $\vec{J} = \sigma_e (\vec{E} + \vec{u} \times \vec{B})$, with electrical conductivity σ_e .

4) MFD assumptions: charge neutral plasma, $\rho^c = 0$, and time invariant \vec{E} , or $\vec{J} = \frac{1}{\mu_e} \vec{\nabla} \times \vec{B}$.

Because of the MFD assumptions in (4), the above set of equations are not technically the "full" set of MFD equations and we will respect this condition by placing an asterisk on the word "full*" used herein. These assumptions essentially remove the Ampere-Maxwell equation from the full set of MFD equations.

The Low Magnetic Reynolds Number Approximation

An ionized flow within an imposed magnetic field can self induce, thus changing the magnitude of the total magnetic field. The relative magnitude of the induced component depends upon the Magnetic Reynolds number, defined by $R_m = u_0 l_0 \sigma_e \mu_e$, where u_0 and l_0 are reference

flow speed. The magnetic diffusion coefficient is given by $\nu_e = \frac{1}{\sigma_e \mu_e}$. For most aerodynamic

flows the gas conductivity is very small and, consequently, ν_e is very large and the magnetic Reynolds number is less than one. In such cases, any self induced magnetic field supposedly rapidly diffuses away, leaving only the imposed magnetic field. This leads to a great simplification in calculating the electro-magnetic effects upon an ionized flow. This approach, *the low magnetic Reynolds approximation approach*, removes the Faraday equation from the MFD equation set and only needs to add a source term to the usual flow equations to include the electro-magnetic field effects. This source term consists of the Lorentz force, $\vec{L}_f = \vec{J} \times \vec{B}$, acting on the momentum of the flow, Joule heating, caused by the flow of electric current through the fluid, plus the magnetic force work terms affecting the energy of the plasma. The equations become

$$\frac{\partial U}{\partial t} + \frac{\partial F}{\partial x} + \frac{\partial G}{\partial y} + \frac{\partial H}{\partial z} = S, \text{ with } S = \left[0, (\vec{J} \times \vec{B})_x, (\vec{J} \times \vec{B})_y, (\vec{J} \times \vec{B})_z, \frac{1}{\sigma_e} \vec{J} \cdot \vec{J} + (\vec{J} \times \vec{B}) \cdot \vec{u} \right]^T$$

Why the Need for the Full* Set of MFD Equations?

C. Park, D.W. Bogdanoff and U.B. Mehta¹ presented a 1-D analysis of the performance of a scramjet propulsion system incorporating the MFD energy bypass concept¹. The MFD accelerator section was a square converging duct, 2.846m long, of height/width 0.933m at the entrance and 0.730m at the exit, part of which is sketched in Fig.1. It is located just down stream of the combustor section. Combustion was not simulated numerically in this study.



Figure 1 Sketch of MFD accelerator simulation

The magnetic field across the channel was $B_0 = 11.28\text{T}$ and the transverse voltage gradient varied from 30,990 V/m at the entrance to 31,470 V/m at the exit. At the entrance the pressure was $1.251 \times 10^6 \text{ N/m}^2$, temperature 3583° K , and the Mach number equaled 1.147. The electrical conductivity was $\sigma_e = 35.87 \text{ mho/m}$. This value was used in the Park, Bogdanoff and Mehta study. The interaction parameter $Q = \sigma_e B_0^2 l_0 / \rho_\infty u_\infty = 20$ and $R_m = 0.17$, based on accelerator channel length. The velocity vectors within the combustor and accelerator sections are shown in Figs.2 and 3. They both show acceleration in accord with the load factor set at 2.04. However, it can also be seen that the velocities are larger in the combustor section for the low magnetic Re number approach.

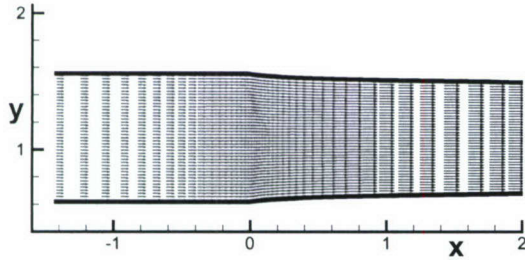


Figure 2 Velocity vectors, low magnetic Re approach

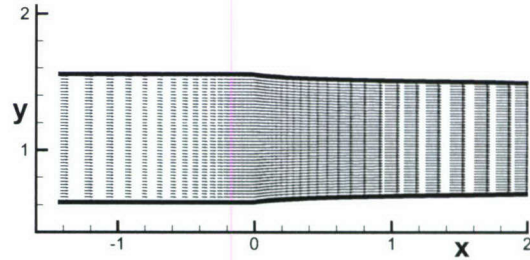


Figure 3 Velocity vectors, full MFD approach

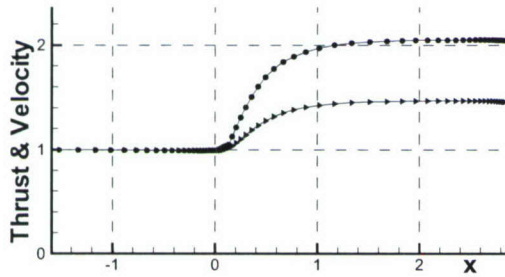


Figure 4 Thrust and velocity, low magnetic Re approach

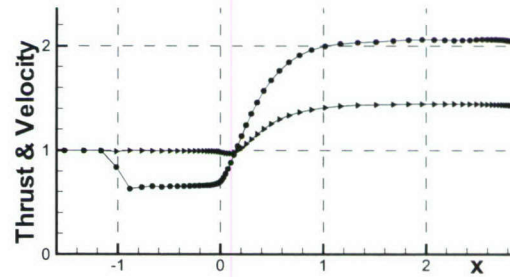


Figure 5 Thrust and velocity, full* MFD approximation

A disturbance that has propagated upstream against the Mach 1.147 flow can be observed in Figs.3 and 5. This can only be a shock wave, which could cause serious engine unstart and was missed by the low magnetic Reynolds number approach.

II. Technical Progress

Numerical Procedures

The following six sections represent numerical procedures that have been devised or further developed during the course of the present contact period. We start by presenting again, though in greater detail, the Full* Set of MFD equations and the Low Magnetic Reynolds Number equations. An additional description that avoids numerical precision difficulties in flow simulations within strong magnetic and electric fields is also described.

(1) The Equations of Magneto-Fluid Dynamics

(i) The Full* Equations of Magneto-Fluid-Dynamics

The unsteady equations of compressible viscous flow within an imposed magnetic field become

$$\frac{\partial U}{\partial t} + \frac{\partial F}{\partial x} + \frac{\partial G}{\partial y} + \frac{\partial H}{\partial z} = 0$$

The state flux vector is given by

$$U = [\rho, \rho u, \rho v, \rho w, e^*, B_x, B_y, B_z]^T$$

with density ρ , velocities u, v and w , total energy per unit volume, including magnetic field energy, $e^* = e + \frac{1}{2\mu_e} B^2$, and B_x, B_y and B_z are the components of the magnetic field. $e = \rho(\varepsilon + \frac{1}{2}(u^2 + v^2 + w^2))$, ε represents the internal energy and $B^2 = B_x^2 + B_y^2 + B_z^2$. The flux vector F becomes

$$F = \begin{pmatrix} \rho u \\ \rho u^2 + p^* + \tau_{xx} - \frac{1}{\mu_e} B_x B_x \\ \rho v u + \tau_{xy} & -\frac{1}{\mu_e} B_x B_y \\ \rho w u + \tau_{xz} & -\frac{1}{\mu_e} B_x B_z \\ (e^* + p^* + \tau_{xx})u + \tau_{xy}v + \tau_{xz}w - k \frac{\partial T}{\partial x} \\ + \frac{1}{\mu_e} \left(-(\vec{B} \cdot \vec{u}) B_x + \beta_{xx} B_x + \beta_{xy} B_y + \beta_{xz} B_z \right) \\ \beta_{xx} \\ B_y u - B_x v + \beta_{xy} \\ B_z u - B_x w + \beta_{xz} \end{pmatrix}$$

with $p^* = p + \frac{1}{2\mu_e} B^2$ and magnetic stress given by $\beta_{ij} = -\nu_e \left(\frac{\partial B_j}{\partial x_i} - \frac{\partial B_i}{\partial x_j} \right)$. The magnetic field components shown above represent the total of the imposed and induced fields. The viscous

stress tensor is given by $\tau_{ij} = -\mu \left(\frac{\partial u_i}{\partial x_j} + \frac{\partial u_j}{\partial x_i} \right) - \delta_{ij} \lambda \frac{\partial u_k}{\partial x_k}$, where δ_{ij} is the Kronecker delta. The other flux vectors G and H are similar. The eigenvalues are for the flux vector F are

$$\lambda_{1,6} = u, \quad \lambda_{3,4} = u \pm \frac{B_x}{\sqrt{\rho}}, \quad \lambda_{2,5} = u \pm \sqrt{\frac{1}{2} \left(c^2 + \frac{B^2}{\rho} + \sqrt{\left(c^2 + \frac{B^2}{\rho} \right)^2 - 4c^2 \frac{B_x^2}{\rho}} \right)} \text{ and}$$

$$\lambda_{7,8} = u \pm \sqrt{\frac{1}{2} \left(c^2 + \frac{B^2}{\rho} - \sqrt{\left(c^2 + \frac{B^2}{\rho} \right)^2 - 4c^2 \frac{B_x^2}{\rho}} \right)}$$

(ii) The Governing Equations Under the Low Magnetic Reynolds Number Approximation

An ionized flow within an imposed magnetic field can self induce, thus changing the magnitude of the total magnetic field. The relative magnitude of the induced component depends upon the Magnetic Reynolds number, defined by $R_m = u_0 l_0 \sigma_e \mu_e$, where u_0 and l_0 are reference flow speed and length, σ_e is the gas electrical conductivity and, $\mu_e = 4\pi \times 10^{-7}$ is the magnetic permeability. The magnetic diffusion coefficient is given by $\nu_e = \frac{1}{\sigma_e \mu_e}$. For most aerodynamic

flows the gas conductivity is very small and, consequently, ν_e is very large and the magnetic Reynolds number is less than one. In such cases, any self induced magnetic field supposedly rapidly diffuses away, leaving only the imposed magnetic field. This leads to a great simplification in calculating the electro-magnetic effects upon an ionized flow. This approach, *The Low Magnetic Reynolds Approximation approach*, only needs to add a source term to the usual flow equations to include the electro-magnetic field effects.

Ionized flow in the presence of a magnetic or electric field generates a current, according to Ohm's law, $\vec{j} = \sigma_e (\vec{E} + \vec{u} \times \vec{B})$, where \vec{j} is the current density, \vec{E} is the electric field potential, \vec{u} is the flow velocity and \vec{B} is the magnetic field. The electric current itself interacts with the magnetic field to create a Lorentz force, $\vec{L}_f = \vec{j} \times \vec{B}$, that acts on the flow in addition to pressure, p , and viscous stress.

In addition to the Lorentz force added to the momentum equations, Joule heating, caused by the flow of electric current through the fluid, plus magnetic force work terms need to be added to the energy equation. The equations become

$$\frac{\partial U}{\partial t} + \frac{\partial F}{\partial x} + \frac{\partial G}{\partial y} + \frac{\partial H}{\partial z} = S$$

The state, flux vectors and the source vector are given by $U = [\rho, \rho u, \rho v, \rho w, e]^T$

$$F = \begin{pmatrix} \rho u \\ \rho u^2 + p + \tau_{xx} \\ \rho v u + \tau_{xy} \\ \rho w u + \tau_{xz} \\ (e + p + \tau_{xx})u + \tau_{xy}v + \tau_{xz}w - k \frac{\partial T}{\partial x} \end{pmatrix}, \text{etc, and } S = \begin{pmatrix} 0 \\ (\vec{j} \times \vec{B})_x \\ (\vec{j} \times \vec{B})_y \\ (\vec{j} \times \vec{B})_z \\ (\vec{j} \times \vec{B}) \cdot \vec{u} + \frac{1}{\sigma_e} \vec{j} \cdot \vec{j} \end{pmatrix}$$

The eigenvalues for the flux vector F , under the low Magnetic Reynolds approximation, are

$$\lambda_{1,3,4} = u \text{ and } \lambda_{2,5} = u \pm c$$

This equation set is supposedly sufficient to describe ionized flow within an electro-magnetic field, as long as the fields are specified. It is not much more difficult to solve than the underlying Navier-Stokes flow equations themselves. However, if the magnetic field varies in time by self induction and the induced magnetic components are relatively significant in magnitude then the equations for magnetic induction also need to be solved. This larger set, shown earlier, is much more difficult to solve and should not be attempted if it can be avoided. However, as shown in the Background section above, this simpler set of equations may not suffice even for aerodynamic flows.

(iii) An Alternative Formulation of the Equations of Magneto-fluid-Dynamics -

The Reduced MFD Equations

An alternate formulation of the governing equations of magneto-fluid-dynamics has been devised. This formulation is mathematically equivalent to the original set of equations governing magneto-fluid-dynamics, given above in Sec.(i), including magnetic self induction, and retains the conservation law form of the equations and their eigenvalues. This new set has advantages over the original set when solved numerically for flows within strong imposed magnetic fields.

This formulation treats the imposed and induced fields separately. Though ever present, the imposed field remains in the background as the finite volume difference equations focus on the induced field. The imposed field can not be eliminated entirely from the difference equations because of non-linearity, but no squared terms of the imposed magnetic field appear. This is important for flows within strong imposed magnetic fields, because the magnetic pressure, proportional to the square of the imposed magnetic field strength, can be several orders of magnitude larger than the aerodynamic pressure or the induced magnetic field pressure. Numerical errors in the very large magnetic stress difference terms of the imposed field could be of significance when combined with the relatively smaller fluid stress terms.

Before the introduction of this alternative formulation, there were two choices for including the effects of a magnetic field upon an ionized flow: (1) the complete equations of magneto-fluid-dynamics, including magnetic induction and diffusion and (2) the inclusion of the “j cross B” force and Joule heating effects in the Navier-Stokes equations as additional source terms. The first choice is a set of eight equations consisting of the Navier-Stokes equations, with added

magnetic stress tensor, plus the Maxwell inductions equations and is presented in Sec.(i) above. The second choice, a set of five equations, called the “Low Magnetic Reynolds Number Approximation”, assumes that the induced magnetic field is negligible. It is far more efficient and has far fewer numerical difficulties associated with inclusion of magnetic effects than the first choice. There is, however, some uncertainty in when the Low Magnetic Reynolds number is valid, even for aerodynamic flows of current interest. The now available third choice presented below is a consistent alternative to the first choice.

The total magnetic field consists of the imposed magnetic field \vec{B}_0 and the induced magnetic field \vec{B}_i . $\vec{B}_t = \vec{B}_0 + \vec{B}_i$, where the subscripts t , 0 and i now and below indicate *total*, *imposed* and *induced* magnetic components. For cases for which the induced field is much less than the imposed field, but not negligibly small, we can benefit by rewriting the Lorentz force as $\vec{L}_f = \frac{1}{\mu_e} (\vec{\nabla} \times \vec{B}_t) \times \vec{B}_t$, because the imposed magnetic field is generated by currents external to

the flow field, for which $\vec{\nabla} \times \vec{B}_0 = 0$. The approach taken here is similar to the simplification in electromagnetic scattering where only the disturbed field is calculated, with nothing lost by the separation of the two fields.

We can also write the Lorentz force as $\vec{L}_f = \frac{1}{\mu_e} (\vec{\nabla} \times \vec{B}_t) \times \vec{B}_t - \frac{1}{\mu_e} (\vec{\nabla} \times \vec{B}_0) \times \vec{B}_0$, and through some algebraic manipulation, the Lorentz force can be brought into the flux derivative terms of the momentum equation, in conservation law form as before. The state vector becomes $U = [\rho, \rho u, \rho v, \rho w, e^*, B_{i_x}, B_{i_y}, B_{i_z}]^T$ and the new flux vector F becomes

$$F = \begin{pmatrix} \rho u \\ \rho u^2 + p^* + \tau_{xx} - \frac{1}{\mu_e} B_{i_x} B_{i_x} v v - \frac{1}{\mu_e} \{B_{i_x} B_{0_x}\} \\ \rho v u + \tau_{xy} - \frac{1}{\mu_e} B_{i_y} B_{i_x} - \frac{1}{\mu_e} \{B_{i_x} B_{0_y}\} \\ \rho w u + \tau_{xz} - \frac{1}{\mu_e} B_{i_z} B_{i_x} - \frac{1}{\mu_e} \{B_{i_x} B_{0_z}\} \\ (e^* + p^* + \tau_{xx})u + \tau_{xy}v + \tau_{xz}w - k \frac{\partial T}{\partial x} \\ + \frac{1}{\mu_e} \left(-(\vec{B}_i \cdot \vec{u}) B_{i_x} + \beta_{xx} B_{i_x} + \beta_{xy} B_{i_y} + \beta_{xz} B_{i_z} \right) \\ \beta_{xx} \\ B_{i_y} u - B_{i_x} v + \beta_{xy} \\ B_{i_z} u - B_{i_x} w + \beta_{xz} \end{pmatrix}$$

with $p^* = p + \frac{1}{2\mu_e} B_t^2 + \frac{1}{\mu_e} \vec{B}_i \cdot \vec{B}_t$ and the magnetic stress given by $\beta_{ij} = -\nu_e \left(\frac{\partial B_{i_j}}{\partial x_i} - \frac{\partial B_{i_i}}{\partial x_j} \right)$

By replacing the magnetic pressure $\frac{1}{2\mu_e} B_t^2$ by the smaller $\frac{1}{2\mu_e} B_i^2 + \frac{1}{\mu_e} \vec{B}_i \cdot \vec{B}_t$, the magnetic and static pressures are closer in magnitude for strong imposed magnetic fields. Favorable reductions also take place in the induction equations because the magnetic diffusion terms β_{ij} are just

components of the curl of the induced magnetic field times ν_e . Again the imposed field, produced by currents outside the flow field, is curl free. Hence, $\nu_e \vec{\nabla} \times \vec{B}_i = \nu_e \vec{\nabla} \times \vec{B}_i$. Here also the production and diffusion terms are more equally balanced. Finally, the terms in the curly brackets in the momentum equations above vanish if the imposed field is constant in space because of the divergence free nature of both the imposed and induced fields.

One may assume that the structural changes to the equations, just presented, from the separation of the induced and imposed fields, would have profound changes to the original eigenvalue-eigenvector structure of the equations. Fortunately, the eigenvalues remain the same as shown below.

$$\lambda_{1,6} = u, \quad \lambda_{3,4} = u \pm \frac{B_{ix}}{\sqrt{\rho}}, \quad \lambda_{2,5} = u \pm \sqrt{\frac{1}{2} \left(c^2 + \frac{B_i^2}{\rho} + \sqrt{\left(c^2 + \frac{B_i^2}{\rho} \right)^2 - 4c^2 \frac{B_{ix}^2}{\rho}} \right)} \text{ and}$$

$$\lambda_{7,8} = u \pm \sqrt{\frac{1}{2} \left(c^2 + \frac{B_i^2}{\rho} - \sqrt{\left(c^2 + \frac{B_i^2}{\rho} \right)^2 - 4c^2 \frac{B_{ix}^2}{\rho}} \right)}$$

The eigenvectors are changed, however, but the original set can still be used in the solution procedure as is to solve the alternative RMFD (Reduced Magneto-Fluid Dynamics) equations just presented, because of the conservation form of the flux vector splitting used.

The term *Reduced* is used here to reflect the notion that the magnitude of the magnetic terms is reduced by removing as often as possible the imposed magnetic field from them, although the number of terms is actually increased. The RMFD equations are mathematically and physically equivalent to the original MFD equations.

(2) Boundary Conditions

(i) At Solid Walls

The usual “no slip” type boundary conditions are used for the Navier-Stokes terms of the governing equations. The boundary conditions for the magnetic terms appearing in the fluid flow equations, i.e., the fluid momentum equations containing the Lorentz force terms and the energy equation containing the Joule heating and magnetic force work terms, are as follows.

- The imposed magnetic field is specified everywhere.
- The normal component of the induced magnetic field is fixed to zero (see note below).
- The tangential components of the induced magnetic field are chosen so that $\vec{\nabla} \times \vec{B}_i = 0$.
-

For the induction equation, $\frac{\partial \vec{B}}{\partial t} = -\vec{\nabla} \times \vec{E} = -\vec{\nabla} \times \left(-\vec{u} \times \vec{B} + \frac{R}{\mu_e} \vec{\nabla} \times \vec{B} \right)$, \vec{E} is specified at the wall.

Note that for perfectly conducting walls ($\sigma_e = \infty$) and the “no slip” boundary condition implying that $\vec{u} = 0$, the tangential components of \vec{E} must vanish, otherwise the current $\vec{J} \approx \sigma_e \vec{E}$ would

be infinite. This implies that the normal component of $\frac{\partial \vec{B}}{\partial t}$ must vanish, proving assertion (b) above.

(ii) At Symmetry Planes, Entrance, Exit and Far Field Boundaries

At planes of flow symmetry reflection boundary conditions are applied. At flow through boundaries the eigenvalues of the equations should be used to determine the dependence of the boundary on the interior of the flow. The equations of MFD have characteristic speeds that differ greatly from the wave speeds of the conventional equations for compressible flow. Boundaries that appear to be supersonic may be actually subsonic boundaries because of fast magnetic waves. This is a significant concern for using the “Low Magnetic Reynolds Number Approximation” approach, which is blind to this boundary condition dependence issue.

(3) Electrical Conductivity and Ohm’s law

Most previous numerical studies for solving the MFD equations used a scalar electrical conductivity. However, a scalar electrical conductivity can not simulate the effects of Hall currents and ion slip. A tensor form for the electrical conductivity of the gas is required and is described below.

(i) Scalar Conductivity

The current density \vec{J} can be defined by Ohm’s law, using a scalar electrical conductivity σ_e , as follows

$$\vec{J} = \sigma_e (\vec{E} + \vec{u} \times \vec{B})$$

The conductivity depends upon the number and mobility of the charged particles, both electrons and ions, present. For air it is usually very small and consequently the magnetic and electric fields required for aerodynamic interaction need to be very large. If we define $\vec{E}' = \vec{E} + \vec{u} \times \vec{B}$, then current density can be written as $\vec{J} = \sigma_e \vec{E}'$. Thus \vec{J} is in the same direction as \vec{E}' . This is not strictly true because particle collisions also can cause the charged particle to drift off this course, the $\vec{E}' \times \vec{B}$ drift, within a plane normal to \vec{B} , which causes the Hall current and ion slip effects and requires the electrical conductivity to be represented as a tensor.

(ii) Tensor Conductivity (following along the discussion in Mitchner and Kruger, *Partially Ionized Gases*²)

Consider a local coordinate system $(\hat{x}, \hat{y}, \hat{z})$, where \hat{z} is in the direction of \vec{B} , \hat{y} is in the direction of \vec{E}' in the plane \perp to \vec{B} and \hat{x} is \perp to both \hat{y} and \hat{z} . Then $\vec{B} = B \hat{z}$, and generalized currents in the \hat{x} – \hat{y} are denoted as $J_{\hat{y}} = \sigma_{\perp} E'_{\hat{y}}$ and $J_{\hat{x}} = \sigma_H E'_{\hat{y}}$, and in the \hat{z} direction by $J_z = \sigma_{\parallel} E'_z$. Consider a second coordinate system (x', y', z') , which represents a coordinate rotation about the \hat{z} axis through a angle θ . Then

$$\begin{aligned} J_{x'} &= \cos \theta J_{\hat{x}} + \sin \theta J_{\hat{y}} \\ J_{y'} &= -\sin \theta J_{\hat{x}} + \cos \theta J_{\hat{y}} \end{aligned}$$

Or

$$\begin{aligned} J_{x'} &= -\sigma_H \cos \theta E_{\hat{y}} + \sigma_{\perp} \sin \theta E_{\hat{y}} = -\sigma_H E_{y'} + \sigma_{\perp} E_{x'} \\ J_{y'} &= \sigma_H \sin \theta E_{\hat{y}} + \sigma_{\perp} \cos \theta E_{\hat{y}} = \sigma_H E_{x'} + \sigma_{\perp} E_{y'} \end{aligned}$$

Or, by defining the electrical conductivity tensor Σ , the current density \vec{J} , via Ohm's law, can be written as

$$\begin{bmatrix} J_{x'} \\ J_{y'} \\ J_{z'} \end{bmatrix} = \underbrace{\begin{bmatrix} \sigma_{\perp} & -\sigma_H & 0 \\ \sigma_H & \sigma_{\perp} & 0 \\ 0 & 0 & \sigma_{\parallel} \end{bmatrix}}_{\Sigma} \begin{bmatrix} E_{x'} \\ E_{y'} \\ E_{z'} \end{bmatrix}$$

The first coordinate system, $(\hat{x}, \hat{y}, \hat{z})$ is aligned with the local magnetic and electric field directions. The second (x', y', z') generalizes the direction within the $\hat{y} - \hat{z}$ plane. We now need to relate these to the computational coordinate system (x, y, z) . We define again the $(\hat{x}, \hat{y}, \hat{z})$ coordinate directions as follows $\vec{\hat{z}} = \vec{b} = \frac{\vec{B}}{|B|}$, $\vec{E}_{\parallel}' = (\vec{E}' \cdot \vec{b}) \vec{b}$, $\vec{E}_{\hat{y}}' = \vec{E}' - \vec{E}_{\parallel}'$, $\vec{\hat{y}} = \vec{e} = \frac{\vec{E}_{\hat{y}}'}{|E_{\hat{y}}'|}$ and $\vec{\hat{x}} = \vec{\hat{y}} \times \vec{\hat{z}} = \vec{d}$. Then, using the orthogonal unit vectors \vec{b} , \vec{e} and \vec{d} defined in the (x, y, z) coordinate system, $\vec{b} = (b_x, b_y, b_z)$, $\vec{e} = (e_x, e_y, e_z)$ and $\vec{d} = (d_x, d_y, d_z)$.

Or

$$\begin{bmatrix} \hat{x} \\ \hat{y} \\ \hat{z} \end{bmatrix} = \underbrace{\begin{bmatrix} d_x & d_y & d_z \\ e_x & e_y & e_z \\ b_x & b_y & b_z \end{bmatrix}}_T \begin{bmatrix} x \\ y \\ z \end{bmatrix} \quad \text{and} \quad \begin{bmatrix} x \\ y \\ z \end{bmatrix} = \underbrace{\begin{bmatrix} d_x & e_x & b_x \\ d_y & e_y & b_y \\ d_z & e_z & b_z \end{bmatrix}}_{T^{-1}} \begin{bmatrix} \hat{x} \\ \hat{y} \\ \hat{z} \end{bmatrix}$$

Similarly,

$$\begin{bmatrix} x' \\ y' \\ z' \end{bmatrix} = \underbrace{\begin{bmatrix} \cos \theta & \sin \theta & 0 \\ -\sin \theta & \cos \theta & 0 \\ 0 & 0 & 1 \end{bmatrix}}_S \begin{bmatrix} \hat{x} \\ \hat{y} \\ \hat{z} \end{bmatrix} \quad \text{and} \quad \begin{bmatrix} \hat{x} \\ \hat{y} \\ \hat{z} \end{bmatrix} = \underbrace{\begin{bmatrix} \cos \theta & -\sin \theta & 0 \\ \sin \theta & \cos \theta & 0 \\ 0 & 0 & 1 \end{bmatrix}}_{S^{-1}} \begin{bmatrix} x' \\ y' \\ z' \end{bmatrix}$$

Starting with the current density defined above $\vec{J} = \Sigma \vec{E}'$, written in the (x', y', z') coordinate system, we can express \vec{J} in the computational coordinate system (x, y, z) , using the transformations S and T , as follows.

$$T^{-1} S^{-1} \begin{bmatrix} J_{x'} \\ J_{y'} \\ J_{z'} \end{bmatrix} = T^{-1} S^{-1} \Sigma S T T^{-1} S^{-1} \begin{bmatrix} E_{x'} \\ E_{y'} \\ E_{z'} \end{bmatrix}$$

Or

$$\begin{bmatrix} J_x \\ J_y \\ J_z \end{bmatrix} = \underbrace{T^{-1} S^{-1} \Sigma S T}_{R^{-1}} \begin{bmatrix} E'_x \\ E'_y \\ E'_z \end{bmatrix} = R^{-1} \begin{bmatrix} E_x + (\vec{u} \times \vec{B})_x \\ E_y + (\vec{u} \times \vec{B})_y \\ E_z + (\vec{u} \times \vec{B})_z \end{bmatrix}$$

Or

$$\begin{bmatrix} E'_x \\ E'_y \\ E'_z \end{bmatrix} = \begin{bmatrix} E_x + (\vec{u} \times \vec{B})_x \\ E_y + (\vec{u} \times \vec{B})_y \\ E_z + (\vec{u} \times \vec{B})_z \end{bmatrix} = \underbrace{T^{-1} S^{-1} \Sigma^{-1} S T}_R \begin{bmatrix} J_x \\ J_y \\ J_z \end{bmatrix}, \text{ where } \Sigma^{-1} = \frac{1}{\sigma_{\perp}^2 + \sigma_H^2} \begin{bmatrix} \sigma_{\perp} & \sigma_H & 0 \\ -\sigma_H & \sigma_{\perp} & 0 \\ 0 & 0 & \frac{\sigma_{\perp}^2 + \sigma_H^2}{\sigma_{\parallel}} \end{bmatrix}$$

and R is the resistivity matrix. Using the MFD assumption, $\vec{J} = \frac{1}{\mu_e} \vec{\nabla} \times \vec{B}$, we can express the electric field as

$$\vec{E} = -\vec{u} \times \vec{B} + \frac{R}{\mu_e} \vec{\nabla} \times \vec{B}$$

The equation for magnetic induction is then

$$\frac{\partial \vec{B}}{\partial t} = -\vec{\nabla} \times \vec{E} = -\vec{\nabla} \times \left(-\vec{u} \times \vec{B} + \frac{R}{\mu_e} \vec{\nabla} \times \vec{B} \right)$$

For the scalar electrical conductivity $R = \frac{1}{\sigma_e}$, otherwise $R = T^{-1} S^{-1} \Sigma^{-1} S T$. The conductivities used within the tensor Σ^{-1} are defined by

$$\sigma_{\perp} = \frac{1+s}{(1+s)^2 + \beta_e^2} \sigma_e, \quad \sigma_H = \frac{\beta_e}{(1+s)^2 + \beta_e^2} \sigma_e \quad \text{and} \quad \sigma_{\parallel} = \sigma_e \quad (1)$$

with

$s = \beta_e \beta_i$, the ion slip factor for a weakly ionized gas,

$\beta_e = \frac{\omega_e}{\nu_e}$, the Hall Parameter for electrons,

$\beta_i = \frac{\omega_i}{\nu_i}$, the Hall Parameter for single charged heavy ions.

The cyclotron (or Larmor) frequency for the electrons, in terms of the magnetic field strength, electron charge and mass, is given by $\omega_e = \frac{|q_e| B}{m_e}$, the corresponding frequency for the ions is

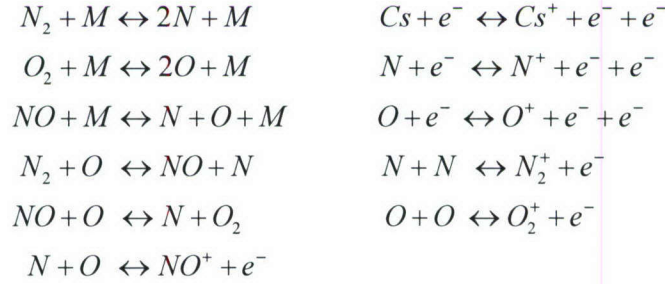
$\omega_i = \frac{|q_i| B}{m_i}$, the average momentum transfer collision frequency for electron is ν_e and that for ions is ν_i . For the present flow simulations $\beta_e = 0.5$ and $\beta_i = 0.05$

(4) Equilibrium Chemistry Model and Evaluation of σ_e

Electrons and ions are created by collisions between the atoms and molecules composing the gas, in our case air and any element introduced into the flow via seeding. The collisions become more violent with increasing temperature. Thus, ionization depends upon the chemical mixture of the gas and temperature. The air chemistry model, with cesium seeding, consisted of 13 species and 11 reactions. The species consisted of

$$N_2, O_2, NO, N, O, Cs, e^-, N_2^+, O_2^+, NO^+, N^+, O^+ \text{ and } Cs^+$$

The reactions 11 considered are



For the cases to be presented cesium seeding was not used. The gas will be assumed to be in chemical equilibrium. Equilibrium coefficients, functions of temperature and particle number densities which determine specie concentrations, were taken from Park's, *Nonequilibrium Hypersonic Aerothermodynamics*³. The local mass fractions were then used as inputs to Park's program "trnpt"⁴ for calculating transport coefficients, including σ_e .

Equilibrium Calculation

The set of species considered above is an open set in that a new species can be added at will. This is different than the usual fixed set of species with temperature and pressure determined from a set of curve fits for the given fixed set of species. However, temperature and pressure must be calculated instead from chemical and thermal equilibrium relations, which is more time consuming. Considerable effort has been made to compute equilibrium conditions efficiently. The flow solver for the governing MFD equations solves the conservation laws for mass, momentum and energy. This determines the fluid density and internal energy at each point of the computational mesh. Temperature and pressure are then determined from the fluid density and internal energy at each point by solving a set of equilibrium relations. The species are ordered by

$$\{s_i\} = \{N_2, O_2, NO, NO^+, N_2^+, O_2^+, N, O, e^-, Cs, Cs^+, N^+, O^+\}$$

The procedure for calculating pressure p and temperature T , given density ρ and internal energy e , at each grid point is as follows.

- 1) The set of concentrations is initialized, $c_i^k = c_i^0 = \rho_i^0 / \rho$, $i = 1, \dots, ns$, where ns is the number of species, ρ_i^0 and c_i^0 are the initial density and concentration of species i and the superscript k indicates the newest value. These initial values correspond to those for

a given reference temperature. For example, for a reference temperature $300^0 K$ with no cesium seeding ,

$$c_1^0 = 0.763, c_2^0 = 0.237, c_{i>2}^0 = 0$$

The reference temperature of $300^0 K$ was chosen in the present calculations. A better choice would be the values for c_i from the previous time step, but this would require significant storage memory, which is avoided at present.

2) The temperature T is initialized by the previous temperature from the last time step at the given grid point and is given by $T^k = T^0$.

3) The set of concentrations $\{c_i^k\}$ consistent with temperature T^k is found by solving a set of equilibrium relations. The number of kg-moles of species i per unit volume is $\chi_i = \rho_i / M_i$, where M_i is the molecular weight in kg of species i . The chemical reactions listed above are of two types

I. Dissociation: molecule AB breaks apart to form species A and B , $AB \leftrightarrow A + B$

The chemical reaction relation is $k_f^I \chi_{AB} \leftrightarrow k_b^I \chi_A \chi_B$, where k_f^I and k_b^I are the forward and backward reaction rates for chemical reaction $AB \leftrightarrow A + B$. In equilibrium this relation becomes $k_f^I \chi_{AB} = k_b^I \chi_A \chi_B$ or $K_{eq}^I \chi_{AB} = \chi_A \chi_B$, where $K_{eq}^I = \frac{k_f^I}{k_b^I}$. The forward

and backward reaction rates were obtained from tabulated values in Park³. They depend upon both particle number density and temperature.

II. Exchange reaction: species A and B form species C and D , $A + B \leftrightarrow C + D$.

Similarly, the equilibrium relation for this reaction is $K_{eq}^{II} \chi_A \chi_B = \chi_C \chi_D$.

Only quadratic equations need to be solved for each reaction equation to bring the concentrations into equilibrium. Consider that an additional x kg-moles/m³ need to react to bring about equilibrium. For a type I chemical reaction the equation is $K_{eq}^I (\chi_{AB} - x) = (\chi_A + x)(\chi_B + x)$, and for type II $K_{eq}^{II} (\chi_A - x)(\chi_B - x) = (\chi_C + x)(\chi_D + x)$. Positive x indicates that the reaction is "forward". Checks need to be made so that the species concentrations remain non-zero. For type I reactions x needs to be bounded by $-\min(\chi_A, \chi_B) \leq x \leq \chi_{AB}$. If $A = B$ then also $-\frac{1}{2} \chi_A \leq x$. For type II reactions $-\min(\chi_C, \chi_D) \leq x \leq \min(\chi_A, \chi_B)$. But if $A = B$, then also $x \leq \frac{1}{2} \chi_A$ and if $C = D$, then also $-\frac{1}{2} \chi_C \leq x$. If x lies outside bound limits it is reset to the nearest limit.

4) The checking of the kg-mole/m³ change x for each reaction in the above step is still not sufficient to avoid negative concentrations. Each reaction was checked independently of the others and when combined may still lead to negative concentrations. A global checking needs to be made. For example species N_2 appears in the first and fourth reactions in column one of the listing above. If $x^{(1)}$ and $x^{(4)}$ indicate changes calculated for each reaction, then the kg-mole/m³ change to N_2 needs to be bounded by $x^{(1)} + x^{(4)} = x_{N_2} \leq \chi_{N_2}$. To insure that all the concentrations remain non-negative we first

set $r_j = 1$, $j = 1, \dots, nr$, where nr is the number of reactions (i.e., $nr = 11$ for the above set of chemical reactions) and denote $x^{(j)}$, $j = 1, \dots, nr$ as the set of kg-mole/m³ changes for the set of chemical reactions. Some of the reactions need to be limited to avoid negative concentrations from occurring. Each species needs to be checked in turn. For example, for the first species, if $x^{(1)} + x^{(4)} = x_{N_2} > \chi_{N_2}$, then the reactions involving N_2 are limited, as follows. $r_1 \leftarrow \min(r_1, \frac{x^{(1)} + x^{(4)}}{\chi_{N_2}})$ and $r_4 \leftarrow \min(r_4, \frac{x^{(1)} + x^{(4)}}{\chi_{N_2}})$. Similarly, for the second species O_2 , which appears in reactions (2) and (5), if $x^{(2)} - x^{(5)} = x_{O_2} > \chi_{O_2}$ (notice the minus sign appearing before $x^{(5)}$, which results from its presence on the “backward” side of the reaction equation), then $r_2 \leftarrow \min(r_2, \frac{x^{(2)} - x^{(5)}}{\chi_{O_2}})$ and $r_5 \leftarrow \min(r_5, \frac{x^{(2)} - x^{(5)}}{\chi_{O_2}})$, etc. After checking each species in turn the set of kg-mole/m³ changes is reset $x^{(j)} \leftarrow r_j x^{(j)}$, $j = 1, \dots, nr$ and each species is adjusted toward equilibrium, for example, $\chi_{N_2} \leftarrow \chi_{N_2} - x^{(1)} - x^{(4)}$ and $\chi_{O_2} \leftarrow \chi_{O_2} - x^{(2)} + x^{(5)}$, etc. The new concentrations become $c_i^{k+1} \leftarrow \alpha M_i \frac{\chi_i}{\rho} + (1 - \alpha) c_i^k$, $i = 1, \dots, ns$, where α is a relaxation parameter, currently taken to be $1/2$.

- 5) The new concentrations will distribute the internal energy differently and the thermodynamic properties of the gas need to be recalculated, as follows. $R = \sum_1^{ns} c_i \frac{R_g}{M_i}$, where R and R_g are the specific and universal gas constants and the superscript k on

the concentrations has been suppressed; $c_v = \sum_1^{ns} c_i \left(\underbrace{\frac{3}{2} \frac{R_g}{M_i}}_{trans} + c_{el_i} \right) + \sum_1^{nds} c_i \left(\underbrace{\frac{R_g}{M_i}}_{rot} + c_{vib_i} \right)$ where

c_v is the specific heat at constant volume, nds is the number of diatomic species (the first nds species in the ordered list). The specific heat of the gas contains contributions from translational, rotational, vibrational and electronic state internal energy and c_{el_i} and c_{vib_i} are functions of temperature T^k . The total internal energy, with concentration set

$\{c_i\}$ at temperature T^k , equals $e^k = c_v T^k + \sum_1^{ns} c_i h f_i^0$, where $h f_i^0$ is the heat of formation

of species i relative to the reference temperature $300^0 K$. If the set of concentrations and temperature T^k are such that $e^k = e$, then we have consistency and we may proceed to the next step (6). If they do not match beyond a reasonable tolerance, we then need to choose a different value for T^k , return to step (3) and iterate until convergence, $e^k \rightarrow e$.

A choice for the new estimate of the temperature is

$$T^k \leftarrow T^k + \text{sign} \left[\min \left(\frac{e^k - e}{c_v + c_{hf}}, 1000^\circ K \right), e^k - e \right], \text{ where } c_{hf} \approx \frac{d \sum_{i=1}^{ns} c_i h f_i^0}{dT^k}$$

- 6) The new temperature becomes the T^k for which $e^k \rightarrow e$ sufficiently. Thus $T = T^k$ and the pressure becomes $p = \rho RT$.

(5) Divergence Control of the Induced Magnetic Field

An important constraint on the magnetic field is that it be divergence free, $\vec{\nabla} \cdot \vec{B} = 0$. During the course of the calculation, error in the numerical solution of the magnetic induction equations, containing both production terms and strong diffusion terms, can cause the magnetic field to drift away from being divergence free. If uncorrected, this can quickly escalate the error in the simulation. There are a few options for controlling this error: (1) a convection term can be retained in the governing equations, proportional to $\vec{\nabla} \cdot \vec{B}$, to carry error out of the flow field, (2) a poisson equation can be setup whose solution can be used to drive the divergence error back toward zero, and (3) the divergence error can be placed in a dissipation equation to attenuate it toward zero. The choice of which procedure to use is very case dependent. Procedure (1) is fairly popular, but causes the governing equations to lose the “conservation law” form. Previously, the present effort used procedure (2) for internal flows with good success. Procedure (3), perhaps better suited for the unbounded external flow, is believed to be a new algorithm improvement and will be presented here. Consider the following three equations in “conservation law” form.

$$\frac{\partial B_x}{\partial t} = \frac{\partial \vec{\nabla} \cdot \vec{B}}{\partial x}, \quad \frac{\partial B_y}{\partial t} = \frac{\partial \vec{\nabla} \cdot \vec{B}}{\partial y} \quad \text{and} \quad \frac{\partial B_z}{\partial t} = \frac{\partial \vec{\nabla} \cdot \vec{B}}{\partial z} \quad (2)$$

If $\vec{\nabla} \cdot \vec{B} = 0$ everywhere, the above equations will not change the magnetic field. On the other hand, if $\vec{\nabla} \cdot \vec{B} \neq 0$, the equations will change the magnetic field, but the new field will also have a changed divergence governed by

$$\frac{\partial \vec{\nabla} \cdot \vec{B}}{\partial t} = \frac{\partial^2 \vec{\nabla} \cdot \vec{B}}{\partial x^2} + \frac{\partial^2 \vec{\nabla} \cdot \vec{B}}{\partial y^2} + \frac{\partial^2 \vec{\nabla} \cdot \vec{B}}{\partial z^2} \quad (3)$$

This equation represents the dissipation equation for the divergence of the magnetic field. The boundary conditions for the above equations are that $\vec{\nabla} \cdot \vec{B} = 0$ along all boundaries. The error introduced within the flow field during a flow simulation probably has both positive and negative values for $\vec{\nabla} \cdot \vec{B}$, occurring in equal measure. The dissipation equation together with the boundary conditions should drive the error toward zero. However, the procedure is numerical and consideration of how the derivative terms above are represented by finite differences is important. Using the notation for backward, forward and central difference operators as follows,

$$\frac{D_- \cdot}{\Delta x} B_x = \frac{B_{x_{i,j,k}} - B_{x_{i-1,j,k}}}{x_i - x_{i-1}}, \quad \frac{D_+ \cdot}{\Delta x} B_x = \frac{B_{x_{i+1,j,k}} - B_{x_{i,j,k}}}{x_{i+1} - x_i} \quad \text{and} \quad \frac{D_0 \cdot}{\Delta x} B_x = \frac{B_{x_{i+1,j,k}} - B_{x_{i-1,j,k}}}{x_{i+1} - x_{i-1}},$$

etc., where the “dots” appearing in the operator notation imply that the operator applies to all factors to the right. The equations above are differenced as follows. First the divergence of the magnetic field is approximated by

$$\vec{\nabla} \cdot \vec{B}_{i,j,k} \approx \frac{D_+ \cdot}{\Delta x} B_{x_{i,j,k}} + \frac{D_+ \cdot}{\Delta y} B_{y_{i,j,k}} + \frac{D_+ \cdot}{\Delta z} B_{z_{i,j,k}}$$

Equations (2) are then approximated by, where the superscript index n indicates the time step,

$$\begin{aligned} \frac{B_{x_{i,j,k}}^{n+1} - B_{x_{i,j,k}}^n}{\Delta t} &= \frac{D_- \cdot}{\Delta x} \vec{\nabla} \cdot \vec{B}_{i,j,k}^n, \quad \frac{B_{y_{i,j,k}}^{n+1} - B_{y_{i,j,k}}^n}{\Delta t} = \frac{D_- \cdot}{\Delta y} \vec{\nabla} \cdot \vec{B}_{i,j,k}^n \quad \text{and} \\ \frac{B_{z_{i,j,k}}^{n+1} - B_{z_{i,j,k}}^n}{\Delta t} &= \frac{D_- \cdot}{\Delta z} \vec{\nabla} \cdot \vec{B}_{i,j,k}^n \end{aligned}$$

Equation (3), though not solved, predicts that the solution to the above difference equations will result in

$$\vec{\nabla} \cdot \vec{B}_{i,j,k}^{n+1} = \vec{\nabla} \cdot \vec{B}_{i,j,k}^n + \Delta t \left\{ \frac{D_+ \cdot}{\Delta x} \frac{D_- \cdot}{\Delta x} \vec{\nabla} \cdot \vec{B}_{i,j,k}^n + \frac{D_+ \cdot}{\Delta y} \frac{D_- \cdot}{\Delta y} \vec{\nabla} \cdot \vec{B}_{i,j,k}^n + \frac{D_+ \cdot}{\Delta z} \frac{D_- \cdot}{\Delta z} \vec{\nabla} \cdot \vec{B}_{i,j,k}^n \right\}$$

which indicates that the new divergence of the magnetic field equals the previous value modified by dissipation.

For the present simulations, Eqs.(2) were solved in a general curvilinear axisymmetric coordinate system. To preserve axisymmetry, central difference operators were used to approximate derivatives in the z direction.

(6) The Numerical Method

The governing equation $\frac{\partial U}{\partial t} + \frac{\partial F}{\partial x} + \frac{\partial G}{\partial y} + \frac{\partial H}{\partial z} = 0$, shown above, contains both inviscid terms and viscous terms. All terms and the boundary conditions are treated implicitly. The inviscid terms, essentially the Euler equations extended to the ideal equations of MFD, use a modified Steger-Warming flux splitting procedure. Assuming, for the moment two dimensional flow and that the flux vectors shown below contain only the inviscid terms, we can write

$$F = AU \quad \text{and} \quad G = BU, \quad \text{where} \quad A = \frac{\partial F}{\partial U} \quad \text{and} \quad B = \frac{\partial G}{\partial U}$$

We can turn these inside out as follows, assuming also for the moment that the inverses exist, (i.e., the eigenvalues of A and B do not vanish).

$$U = A^{-1}F \text{ and } U = B^{-1}G, \text{ where } A^{-1} = S^{-1}C_A^{-1}\Lambda_A^{-1}C_AS \text{ and } B^{-1} = S^{-1}C_B^{-1}\Lambda_B^{-1}C_BS$$

Therefore, we can split the fluxes F and G directly as follows

$$\begin{aligned} F_{\pm} &= S^{-1}C_A^{-1}\Lambda_{A_{\pm}}^{-1}C_AS F = S^{-1}C_A^{-1}D_{A_{\pm}}C_AS F = \mathcal{A}_{\pm}F \\ &\text{and} \\ G_{\pm} &= S^{-1}C_B^{-1}\Lambda_{B_{\pm}}^{-1}C_BS G = S^{-1}C_B^{-1}D_{B_{\pm}}C_BS G = \mathcal{B}_{\pm}G \end{aligned}$$

where the diagonal matrices $D_{A_{\pm}}$ and $D_{B_{\pm}}$ have “ones” or “zeros” as elements. For example, D_{A_+} has “ones” where Λ_{A_+} has non-zero elements and $D_{A_-} = I - D_{A_+}$. This approach has the benefit of partitioning the conservative flux vectors themselves, which, for example, unlike the state vectors, are often continuous across discontinuities in the flow. In terms of the generic flux vectors

$$F_{i+1/2,j}^n = \mathcal{A}_{+,j}^n F_{i,j}^n + \mathcal{A}_{-,j}^n F_{i+1,j}^n \quad \text{and} \quad G_{i,j+1/2}^n = \mathcal{B}_{+,j}^n G_{i,j}^n + \mathcal{B}_{-,j+1}^n G_{i,j+1}^n$$

Higher order accurate approximations for the fluxes can be made by upwind extrapolation or interpolation of the flow variables to the flux surfaces. i.e.,

$$F_{i+1/2,j}^n = \mathcal{A}_{+,j}^n F_R^n + \mathcal{A}_{-,j}^n F_L^n, \text{ etc.}$$

The method used herein was third order accurate in space and, because the flows converged in time to a steady state, only first order accurate in time. The method is also TVD (Total Variation Diminishing) to be discussed below. Also, the full set of Navier-Stokes viscous terms, plus the magnetic dispersion terms, $\nu_e \vec{\nabla} \times \vec{B}$, of the Faraday equation, were included using second order accurate central difference approximations.

TVD (Total Variation Diminishing) Method Extension

We present the extension to TVD of the Modified Steger-Warming Method. This extension is more than cosmetic. It is designed to prevent spurious oscillation in the solution that can cause severe numerical difficulties. We illustrate the procedure by applying it to the Euler equations in conservative form in one spatial dimension, as follows. The Euler equations are

$$\frac{\partial U}{\partial t} + \frac{\partial F}{\partial x} = 0, \text{ where } U = \begin{pmatrix} \rho \\ \rho u \\ e \end{pmatrix} \text{ and } F = \begin{pmatrix} \rho u \\ \rho u^2 + p \\ (e + p)u \end{pmatrix}$$

A generic algorithm for solving these equations is

$$U_i^{n+1} = U_i^n - \frac{\Delta t}{\Delta x} \{F_{i+1/2}^n - F_{i-1/2}^n\}$$

The Roe and Modified Steger Warming methods for evaluating the flux vector are shown below. They are both first order methods at present.

$$F_{i+1/2}^n = \begin{cases} F_{i+1/2}^{(Roe)} = \frac{F_i + F_{i+1}}{2} - \frac{1}{2} |\hat{A}_{i+1/2}| (U_{i+1} - U_i) \\ F_{i+1/2}^{(M-S-W)} = \bar{\mathcal{A}}_{+i+1/2} F_i + \bar{\mathcal{A}}_{-i+1/2} F_{i+1} \end{cases}$$

Where we define $|\hat{A}| = \hat{A}_+ - \hat{A}_-$, $\hat{A}_\pm = \hat{S}^{-1} \hat{C}_A^{-1} \hat{\Lambda}_{A_\pm} \hat{C}_A \hat{S}$ and

$$\bar{\mathcal{A}}_\pm = \bar{S}^{-1} \bar{C}_A^{-1} \bar{\Lambda}_{A_\pm} \bar{C}_A \bar{S} = \bar{S}^{-1} \bar{C}_A^{-1} \bar{D}_{A_\pm} \bar{C}_A \bar{S}$$

The “hats” and “bars” indicate that matrices use, respectively, either “Roe” averaged data or arithmetic averaged data. Note that after some algebraic manipulation the Modified Steger Warming method above can be written in a similar form as the Roe method

$$\begin{aligned} F_{i+1/2}^{(M-S-W)} &= \bar{\mathcal{A}}_{+i+1/2} F_i + \bar{\mathcal{A}}_{-i+1/2} F_{i+1} \\ F_{i+1/2}^{(M-S-W)} &= -\frac{1}{2} \bar{\mathcal{A}}_{+i+1/2} (F_{i+1} - F_i) + \frac{1}{2} \bar{\mathcal{A}}_{-i+1/2} (F_{i+1} - F_i) \\ &\quad + \frac{1}{2} \bar{\mathcal{A}}_{+i+1/2} (F_{i+1} + F_i) - \frac{1}{2} \bar{\mathcal{A}}_{-i+1/2} (F_{i+1} + F_i) \\ F_{i+1/2}^{(M-S-W)} &= \underbrace{\left(\bar{\mathcal{A}}_{+i+1/2} + \bar{\mathcal{A}}_{-i+1/2} \right)}_I \frac{F_i + F_{i+1}}{2} - \frac{1}{2} \underbrace{\left(\bar{\mathcal{A}}_{+i+1/2} - \bar{\mathcal{A}}_{-i+1/2} \right)}_{|\bar{\mathcal{A}}_{i+1/2}|'} (F_{i+1} - F_i) \end{aligned}$$

or

$$F_{i+1/2}^{(M-S-W)} = \frac{F_i + F_{i+1}}{2} - \frac{1}{2} |\bar{\mathcal{A}}_{i+1/2}|' (F_{i+1} - F_i)$$

The TVD expression for the second order accurate flux approximation using the Modified Steger-Warming method is

$$\bar{F}_{i+1/2}^n = \bar{\mathcal{A}}_{+i+1/2} \left\{ F_i^n + \frac{1}{2} \left(I - \bar{A}_{+i+1/2} \frac{\Delta t}{\Delta x} \right) (F_i^n - F_{i-1}^n) \right\} + \bar{\mathcal{A}}_{-i+1/2} \left\{ F_{i+1}^n - \frac{1}{2} \left(I + \bar{A}_{-i+1/2} \frac{\Delta t}{\Delta x} \right) (F_{i+2}^n - F_{i+1}^n) \right\}$$

The matrix $\bar{\mathcal{A}}_\pm$ can be diagonalized as follows $\bar{\mathcal{A}}_\pm = \bar{S}^{-1} \bar{C}_A^{-1} \bar{D}_\pm \bar{C}_A \bar{S}$. Therefore we can write flux vector as

$$\begin{aligned}\bar{F}_{i+1/2}^n &= \bar{\mathcal{Q}}_{+,i+1/2} F_i^n + \bar{\mathcal{Q}}_{-,i+1/2} F_{i+1}^n + \frac{1}{2} \bar{S}_{i+1/2}^{-1} \bar{C}_{A,i+1/2}^{-1} \bar{D}_{+,i+1/2} \bar{C}_{A,i+1/2} \bar{S}_{i+1/2} \left(I - \bar{A}_{+,i+1/2} \frac{\Delta t}{\Delta x} \right) (F_i^n - F_{i-1}^n) \\ &\quad - \frac{1}{2} \bar{S}_{i+1/2}^{-1} \bar{C}_{A,i+1/2}^{-1} \bar{D}_{-,i+1/2} \bar{C}_{A,i+1/2} \bar{S}_{i+1/2} \left(I + \bar{A}_{-,i+1/2} \frac{\Delta t}{\Delta x} \right) (F_{i+2}^n - F_{i+1}^n)\end{aligned}$$

or

$$\begin{aligned}\bar{F}_{i+1/2}^n &= \bar{\mathcal{Q}}_{+,i+1/2} F_i^n + \bar{\mathcal{Q}}_{-,i+1/2} F_{i+1}^n + \frac{1}{2} \bar{S}_{i+1/2}^{-1} \bar{C}_{A,i+1/2}^{-1} \bar{D}_{+,i+1/2} \left(I - |\bar{\Lambda}_{+,i+1/2}| \frac{\Delta t}{\Delta x} \right) \bar{C}_{A,i+1/2} \bar{S}_{i+1/2} (F_i^n - F_{i-1}^n) \\ &\quad - \frac{1}{2} \bar{S}_{i+1/2}^{-1} \bar{C}_{A,i+1/2}^{-1} \bar{D}_{-,i+1/2} \left(I - |\bar{\Lambda}_{-,i+1/2}| \frac{\Delta t}{\Delta x} \right) \bar{C}_{A,i+1/2} \bar{S}_{i+1/2} (F_{i+2}^n - F_{i+1}^n)\end{aligned}$$

Let the eigenvalues of \bar{A} be ordered as $\bar{\lambda}_1 = \bar{u}$, $\bar{\lambda}_2 = \bar{u} + \bar{c}$ and $\bar{\lambda}_3 = \bar{u} - \bar{c}$, then

$$\bar{D}_{\pm} = \begin{bmatrix} d_{\pm,1} & 0 & 0 \\ 0 & d_{\pm,2} & 0 \\ 0 & 0 & d_{\pm,3} \end{bmatrix} = \frac{1}{2} \begin{bmatrix} 1 \pm \text{sgn}(\bar{\lambda}_1) & 0 & 0 \\ 0 & 1 \pm \text{sgn}(\bar{\lambda}_2) & 0 \\ 0 & 0 & 1 \pm \text{sgn}(\bar{\lambda}_3) \end{bmatrix}$$

We define the vector G_k for $k = i-1, i, i+1$ and $i+2$ to $i = k+1$, by

$$G_k = \begin{bmatrix} g_1 \\ g_2 \\ g_3 \end{bmatrix}_k = \bar{C}_{A,i+1/2} \bar{S}_{i+1/2} F_k^n, \quad$$

Then

$$\begin{aligned}\bar{F}_{i+1/2}^n &= \bar{S}_{i+1/2}^{-1} \bar{C}_{A,i+1/2}^{-1} \left\{ \bar{D}_{+,i+1/2} G_i + \bar{D}_{-,i+1/2} G_{i+1} + \frac{1}{2} \bar{D}_{+,i+1/2} \left(I - |\bar{\Lambda}_{+,i+1/2}| \frac{\Delta t}{\Delta x} \right) (G_i - G_{i-1}) \right. \\ &\quad \left. - \frac{1}{2} \bar{D}_{-,i+1/2} \left(I - |\bar{\Lambda}_{-,i+1/2}| \frac{\Delta t}{\Delta x} \right) (G_{i+2} - G_{i+1}) \right\}\end{aligned}$$

We now apply the flux limiter to define the TVD flux for the Modified Steger-Warming method.

$$F_{i+1/2}^n = \hat{S}_{i+1/2}^{-1} \hat{C}_{A,i+1/2}^{-1} \begin{bmatrix} d_{+,1} g_{1,i} + d_{-,1} g_{1,i+1} + \frac{1}{2} \left(1 - |\bar{\lambda}_{1,i+1/2}| \frac{\Delta t}{\Delta x} \right) (d_{+,1} \psi_+(g_{1,i} - g_{1,i-1}) - d_{-,1} \psi_+(g_{1,i+1} - g_{1,i})) \\ d_{+,2} g_{2,i} + d_{-,2} g_{2,i+1} + \frac{1}{2} \left(1 - |\bar{\lambda}_{2,i+1/2}| \frac{\Delta t}{\Delta x} \right) (d_{+,2} \psi_+(g_{2,i} - g_{2,i-1}) - d_{-,2} \psi_+(g_{2,i+1} - g_{2,i})) \\ d_{+,3} g_{3,i} + d_{-,3} g_{3,i+1} + \frac{1}{2} \left(1 - |\bar{\lambda}_{3,i+1/2}| \frac{\Delta t}{\Delta x} \right) (d_{+,3} \psi_+(g_{3,i} - g_{3,i-1}) - d_{-,3} \psi_+(g_{3,i+1} - g_{3,i})) \end{bmatrix}$$

where

$$\psi_+(g_{l,i} - g_{l,i-1}) = \min \text{mod} (g_{l,i} - g_{l,i-1}, g_{l,i+1} - g_{l,i})$$

An example of a program for calculating the flux $F_{i+1/2}^n$ at all interior surfaces, from $i = 1 + 1/2$ to $i = I - 1/2$, using temporary variables h_l , for $l = 1, 2$ and 3 , and vectors G_k , with elements $g_{k,l}$, for $k = 1, 2, 3$ and 4 and $l = 1, 2$ and 3 , etc, follows.

- 1) Begin for $i = 1, \dots, I - 1$ do the following
- 2) Calculate $G_1 = \bar{C}_{A_{i+1/2}} \bar{S}_{i+1/2} F_{i'-1}^n$, where $i' = \max(2, i)$
- 3) Calculate $G_2 = \bar{C}_{A_{i+1/2}} \bar{S}_{i+1/2} F_i^n$
- 4) Calculate $G_3 = \bar{C}_{A_{i+1/2}} \bar{S}_{i+1/2} F_{i+1}^n$
- 5) Calculate $G_4 = \bar{C}_{A_{i+1/2}} \bar{S}_{i+1/2} F_{i''+2}^n$, where $i'' = \min(I - 2, i)$
- 6) Calculate, for $l = 1, 2$ and 3 ,

$$\text{if } \text{sgn}(\hat{\lambda}_{l,i+1/2}) = 1 \text{ then } h_l = g_{2,l} + \frac{1}{2} \left(1 - \left| \bar{\lambda}_{l,i+1/2} \right| \frac{\Delta t}{\Delta x} \right) \min \text{mod}(g_{2,l} - g_{1,l}, g_{3,l} - g_{2,l})$$

$$\text{else } h_l = g_{3,l} - \frac{1}{2} \left(1 - \left| \bar{\lambda}_{l,i+1/2} \right| \frac{\Delta t}{\Delta x} \right) \min \text{mod}(g_{3,l} - g_{2,l}, g_{4,l} - g_{3,l}),$$

$$7) \text{ Calculate } F_{i+1/2}^n = \bar{S}_{i+1/2}^{-1} \bar{C}_{A_{i+1/2}}^{-1} \begin{bmatrix} h_1 \\ h_2 \\ h_3 \end{bmatrix}$$

- 8) End if $i = I - 1$

The figure below shows the results for the Modified Steger-Warming method with TVD for flow within a shock tube.

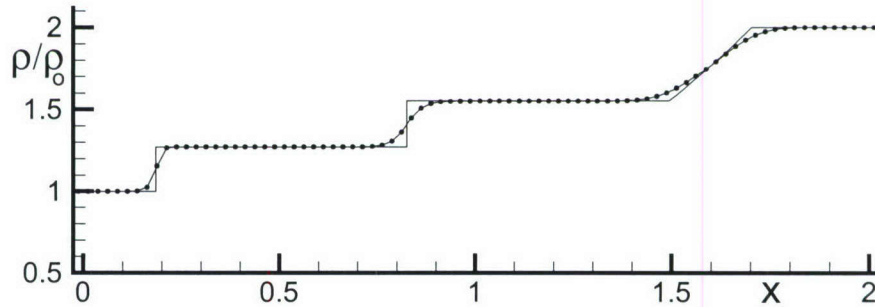


Figure 6 Density comparison for the Modified Steger-Warming method, with TVD, for a moving shock wave, contact discontinuity and rarefaction, (CFL=0.9, 40 time steps)

III. Applications

(1) External Flow: Simulation of the Ziemer Experiment

In 1959 R.W. Ziemer⁵ reported results from an experimental investigation in magneto-aerodynamics. He placed a hemi-spherically nosed cylinder, of diameter 0.02m and made of Pyrex glass, within an electromagnetic shock tube producing a hypervelocity flow of ionized air. He observed that with the magnetic field turned on the shock wave standoff distance increased by a factor of 7.5 for a magnetic interaction parameter $Q = \sigma_1 B_0^2 r_{bdy} / \rho_\infty u_\infty = 69$. The assumed free stream conditions are

velocity	5690 m/s
pressure	3033 N/m ²
temperature	9813 °K
density	$5.847 \times 10^{-2} \text{ kg/m}^3$

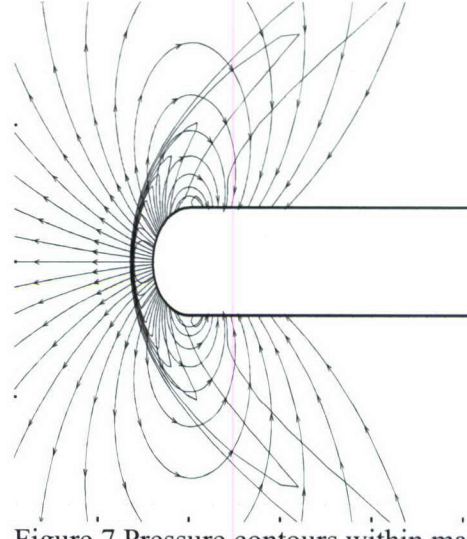


Figure 7 Pressure contours within magnetic field $B_0=2\text{T}$

A discharge of electric current was used first to ionize the air at one end of a 3 inch diameter Pyrex glass pipe and was then followed by a further large capacitor discharge through the ionized gas. The large joule heating of the gas, plus the self pinching of the gas by the large magnetic field created by the current flow, produced a strong shock wave that traveled down the glass pipe toward the test section. A high speed camera was used to record the passage of the shock front past the model and during the establishment of steady equilibrium gas flow. A bow shock wave formed, dividing the shock layer about the model from free stream ahead. A dipole-like magnetic field was created by a current pulse through the copper coil located within the model, which interacted with the surrounding ionized flow.

The magnetic interaction parameter is defined by $Q = \sigma_1 B_0^2 r_{bdy} / \rho_\infty u_\infty$, where σ_1 is the electrical conductivity of the gas within the shock layer, B_0 is the strength of the dipole at the stagnation point, r_{bdy} is the body radius, ρ_∞ is the free stream density and u_∞ is the free stream velocity. The shock wave standoff distance was observed to increase by a factor of 7.5 with $Q=69$ over that with $B_0 = 0$.

Bush Analysis

Bush⁶ cleverly simplified the set of governing equations into an ordinary differential equation and found a similarity solution. He modeled the low subsonic flow in the stagnation region of the shock layer as incompressible, assumed a spherical shock wave shape, initialized the solution at the shock and marched it toward the body. He also assumed that the electrical conductivity

was constant within the shock layer and zero outside of it. His analytical results supported Ziemer's experimental observations and predicted a reduction in heat transfer through magnetic field interaction.

Poggie and Gaitonde Computation

Poggie and Gaitonde⁷ used the theoretical analysis of Bush for validating their computer program developed for solving the equations of magneto-fluid dynamics using the low magnetic Reynolds number approach. This approach fixes the magnetic field to that imposed. The magnetic field interacts with the flow through Lorentz forces and joule heating, modeled through source terms added to the Navier-Stokes equations. Their simulations, using perfect gas relations, agreed well with Bush's theory, thus providing validation for their numerical procedures.

Present Study

The purpose of the present study is the development of numerical procedures to simulate the interaction of strong magnetic and electric fields with weakly ionized aerodynamic flows. The current within the fluid can induce an additional magnetic field, which is governed by the set of Maxwell equations. The complete Navier-Stokes equations, with magnetic stress and energy terms included, plus Maxwell's equations are solved together, subject to the usual MFD assumptions of charge neutrality and that the current density is proportional to the curl of the magnetic field. This set will be called the full equations of magneto-fluid dynamics (MFD) herein, although a larger set without the MHD approximations is more accurately termed the full set. Ziemer's experiment is used herein as a difficult challenge for algorithm development and flow simulation. Although the simulation to be presented is expected to be closer to reality than those of Bush and Poggie and Gaitonde, it is still limited as will be explained below.

The full set of MFD equations, Ohm's for conducting gases, and the equilibrium chemistry model were used in the following simulations. A blast wave moved at Mach 21.5 into stationary air, at temperature 273° K and pressure 9.33N/m², past the model. The free stream Mach number for the flow behind the blast wave, relative to the model, was of 2.0. The free stream conditions are given in the table below. Although an attempt was made to match the experimental conditions of Ziemer, no precise match for the magnetic interaction parameter Q could be made because of the large variation in electrical conductivity behind the shock. There was no clear choice in which value to use. The imposed magnetic field at the stagnation point was $B_0=0, 1$ or 2 Tesla. The temperature behind the shock wave near the nose was about 23,000 °K and pressures were as high as 2×10^4 N/m². At these conditions the flow was almost completely dissociated. The chemistry model, shown above, should also have included doubly ionized molecules and atoms, which limits to some degree the realism of the present simulation. The present chemistry model should be sufficient for temperatures less than 15,000 °K, which would cover the main region of current hypersonic flow interest. Because the main purpose of the present simulation is to challenge the algorithm in development and because the extension to doubly ionized atoms and molecules is very challenging in itself, the chemistry model has not at present been further extended. An isothermal wall boundary condition was assumed with the wall temperature at 273°K.

The equation for the magnetic dipole is

$$\vec{B} = B_0 \frac{r_{bdy}^3}{r^3} \cos \theta \vec{e}_r + B_0 \frac{r_{bdy}^3}{2r^3} \sin \theta \vec{e}_\theta,$$

where r is measured from the origin, θ is measured from the negative x -axis direction, B_0 is the dipole strength and r_{bdy} is the body radius. The dipole should fall off in strength away from the body along the axis of symmetry as $B = B_0 (r_{bdy}/r)^3$. However, Ziemer measured a faster fall off rate of $B = B_0 (r_{bdy}/r)^{3.61}$ in his experiment.

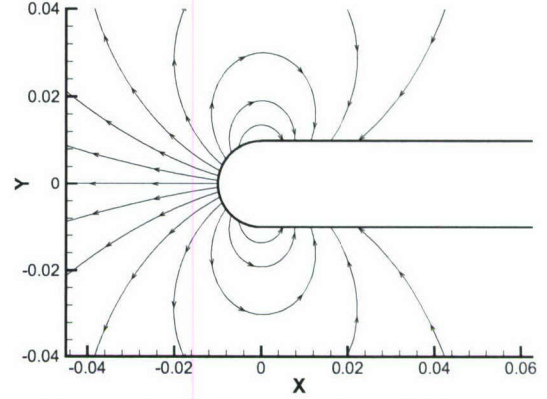


Figure 8 Dipole magnetic field lines

Standoff Distance

The pressure contours for flow about the model are shown below in Figs.9-11, with the results for the full set of MFD equations at the top half of each figure and those for the low magnetic Reynolds number approach below. The standoff distance of the bow shock wave from the model is compared for each approach versus magnetic dipole strength in Fig. 12, with the dashed curve indicating the low magnetic Reynolds number approach.

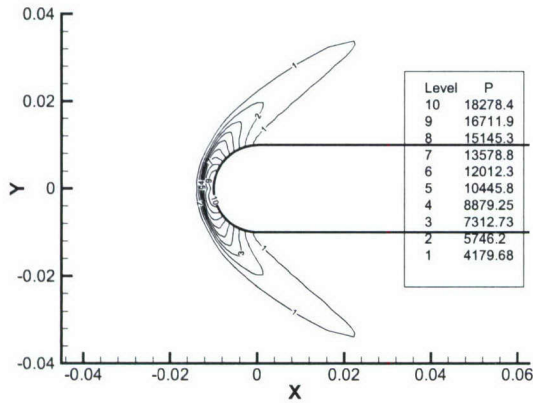


Figure 9 Pressure contours, $B_0=0$

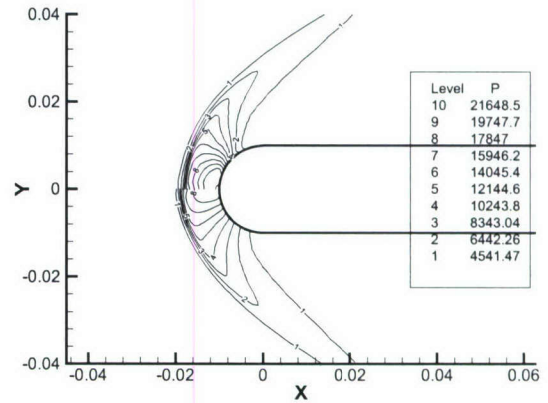


Figure 10 Pressure contours, $B_0=1$

Assuming that the numerical simulations are realistic, it is clear from the above figures that the two approaches yield slightly different standoff distances and pressure contour results, as seen in Figs.10 and 11. To explain this difference we can observe the imposed and induced magnetic fields shown below in Figs.13-16. The maximum induced magnetic field is less than 5% of the imposed magnetic field dipole strength and it falls off at a slower rate with distance

from the body The induced field is in general of opposite sign to that imposed, which in effect cancels part the imposed field and lessens its effect on the bow shock wave standoff distance.

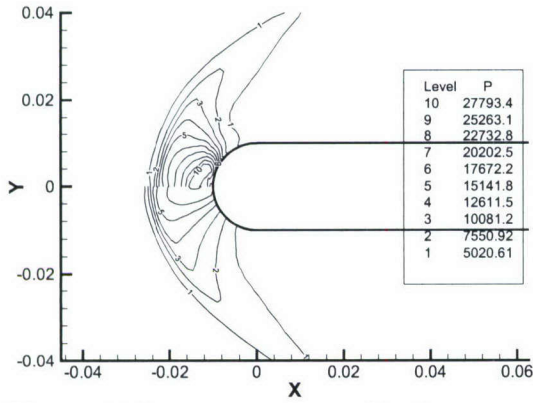


Figure 11 Pressure contours, $B_0=2$

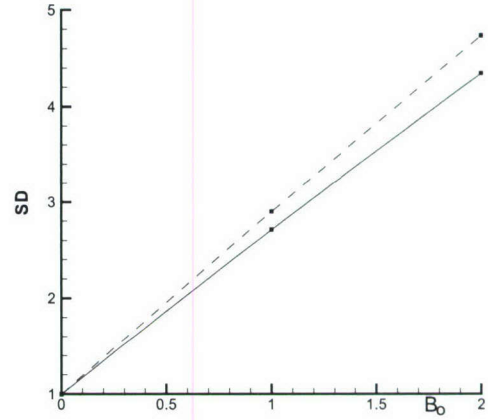


Figure 12 Standoff distance vs. dipole strength

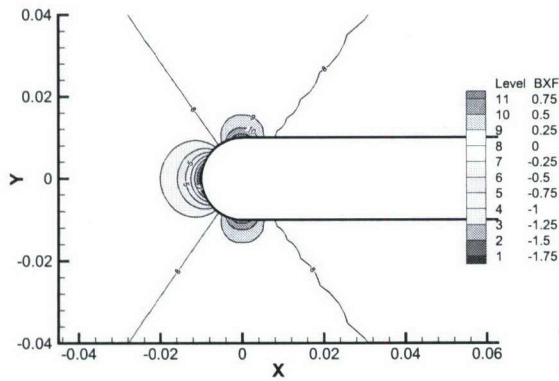


Figure 13 Imposed B_x field, $B_0=2$

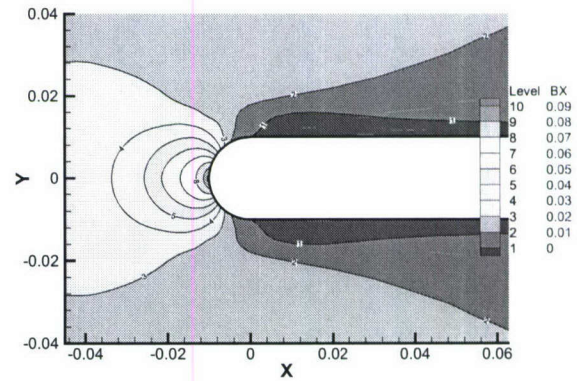


Figure 14 Induced B_x field, $B_0=2$

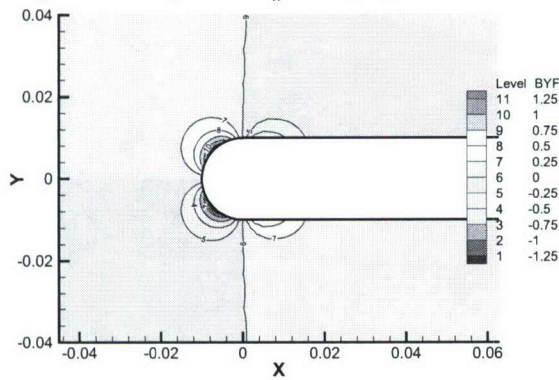


Figure 15 Imposed B_y field, $B_0=2$

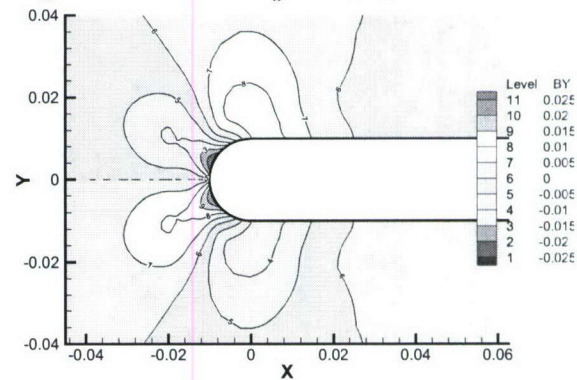


Figure 16 Induced B_y field, $B_0=2$

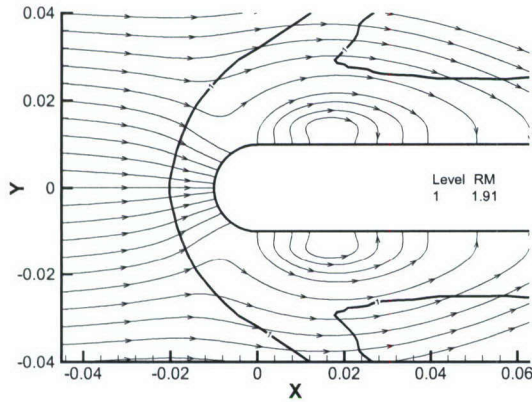


Figure 17 Induced magnetic field lines,
 $B_0=1$

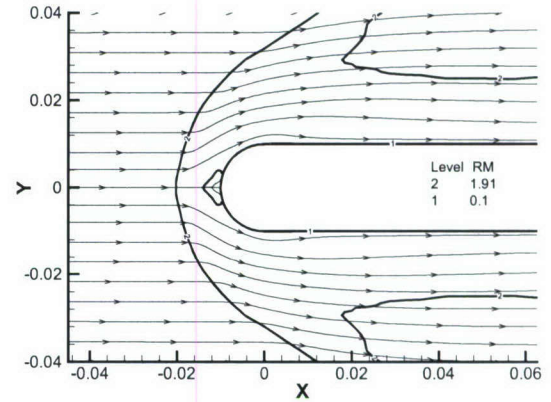


Figure 18 Streamlines, $B_0=1$, full MFD
Eqs.

Fig.17 shows the induced magnetic field lines for the imposed dipole strength $B_0=1$ case. Note the similarity with the streamlines shown in Fig.18. The dark lines in these two figures are Mach contours used to indicate the position of the bow shock wave and regions of low speed flow. The Mach 1.91 is used to indicate the shock wave, but it also reenters the figure downstream of the shock wave as a simple Mach contour. The Mach 0.1 contour appears in Fig.18. Streamlines entering within it are not accurately placed.

Compare the direction of the magnetic field lines in Fig.17 for the induced field with those of Fig.8 for the imposed field. Note they are opposite in direction ahead of the body. The Faraday equation can be written as

$$\frac{\partial \vec{B}}{\partial t} = \vec{\nabla} \times \left(\underbrace{\vec{u} \times \vec{B}}_{\text{production}} - \underbrace{\frac{1}{\sigma_e \mu_e} \vec{\nabla} \times \vec{B}}_{\text{diffusion}} \right) \quad (4)$$

The production term above will continue to change the induced magnetic field until $\vec{u} \times \vec{B} = \vec{0}$, that is until the flow and combined magnetic field are aligned. Note the near alignment between the two in Figs.17 and 18. The pinching of the induced magnetic field lines in Fig.17 counteracts the expansion of those in Fig.8. The diffusion term in Eq.(4) is exceedingly strong for most aerodynamic flows because of the in general small values of the electrical conductivity.

The Hall and Ion Slip Effect

The Hall and ion slip effects tend to reduce the scalar electrical conductivity, as seen in Eq.(1). This can significantly reduce the interaction of the magnetic field with the flow. Figs.19 and 20 show the pressure contours for $B_0=2$ for both the full MFD and low magnetic Re approaches, with the Hall and ion slip results at the top half of the figures and the scalar electrical conductivity results at the bottom half of the figures.

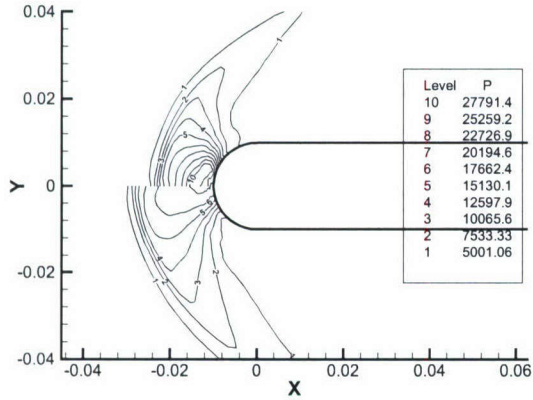


Figure 19 Pressure contours with and without Hall and ion slip effect, full MFD, $B_0=2$

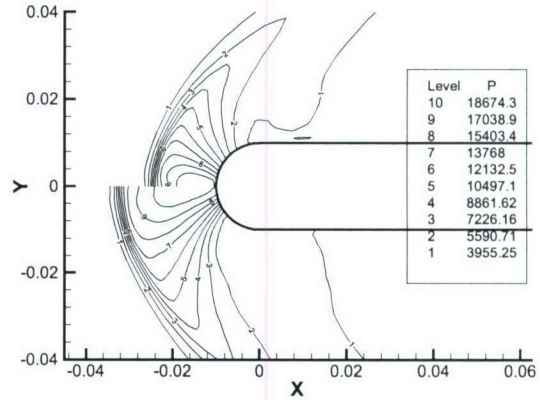


Figure 20 Pressure contours with and without Hall and ion slip effect, low mag. Re, $B_0=2$

Drag

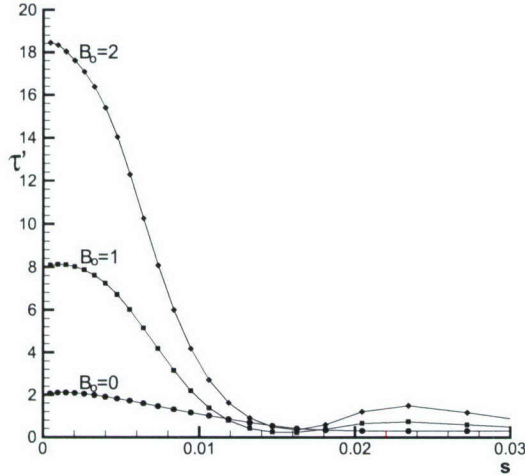


Figure 21 Normal surface stress, full MFD Eqs.

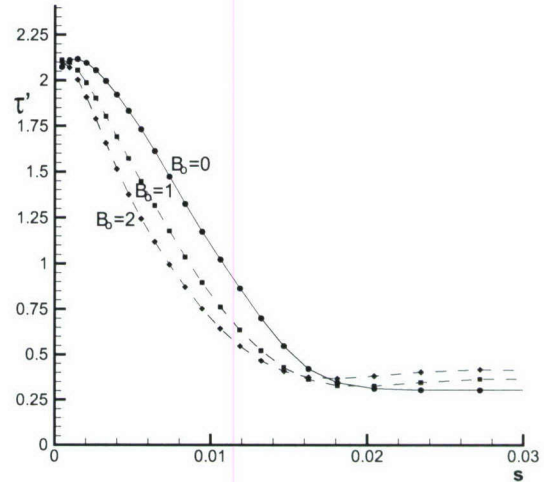


Figure 22 Normal surface stress, low mag. Re Eqs.

The surface stress, normalized by the dynamic pressure of the free stream, versus distance along the body from the stagnation point, is shown in Fig.21 for the full set of MFD equations. The hemisphere-cylinder junction is at $s=0.0157$. These equations are written in “conservation law form” (divergence form) and the force acting on the body surface, both aerodynamic (pressure and viscous stress) and magnetic, are applied directly at the body surface. On the other hand, the set of equations for the low magnetic Reynolds number approach, using source terms to include the magnetic effects, applies magnetic forces on the body as “acting at a distance”. Fig.22 shows the normal stress, along the body surface for the low magnetic Reynolds number approach. Viscous stress was not significant for these simulations. Notice that the magnitudes of normal surface stress for the two approaches are widely different. One could misinterpret drag

acting on the body from consideration of these two figures only. The full MFD equation approach correctly predicts increased drag with increased imposed magnetic dipole strength. Fig.22 for the low magnetic Reynolds number approach does not show this same trend because most of the magnetic force drag occurs via “action at a distance”. Note the large change in scale of the stress axes in these two figures below.

The drag coefficients for each approach were calculated as follows.

For the full MFD equation approach

$$c_{d_{MFD}} = \frac{\text{total axial surface stress}}{\frac{1}{2} \rho_{\infty} u_{\infty}^2 \pi r_{bdy}^2} \quad \text{and}$$

For the low magnetic Reynolds number approach

$$c_{d_{lowRe_{mag}}} = \frac{\text{total axial surface stress} + \text{total axial volume force}}{\frac{1}{2} \rho_{\infty} u_{\infty}^2 \pi r_{bdy}^2}$$

where the “total axial volume force” includes the Lorentz source terms integrated over the fluid volume surrounding the body. The Lorentz force field is shown near the stagnation point in Fig.23 for the low magnetic Reynolds number approach. It appears to focus the flow toward the stagnation point and trap it ahead of the body. The c_d results are shown for both approaches in Fig.24, with the low magnetic Reynolds number approach results connected by the dashed line. The figure shows that the drag coefficient is proportional to the increase in the shock layer volume, caused by the increase in shock standoff distance.

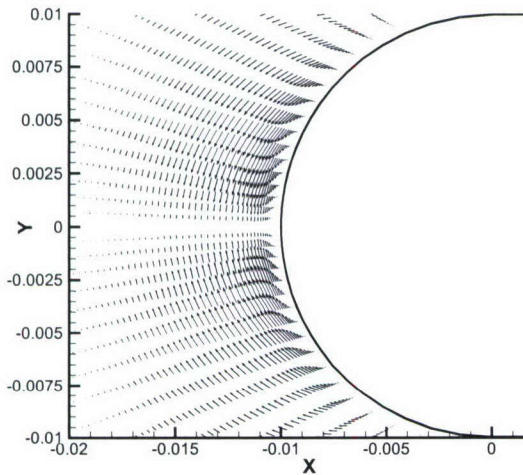


Figure 23 Lorentz force field, low Re_{mag} Eqs., $B_0=1$

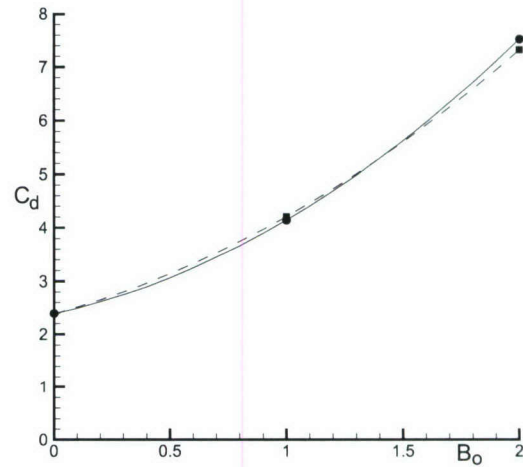


Figure 24 c_d vs. dipole strength

Heat Transfer

As can be seen in Figs.25 and 26, the two approaches predict different rates of heat transfer, though both predict decreases in heat transferred to the body with increased imposed magnetic dipole strength. The normalized values of heat transfer plotted in the figures are given by

$$\dot{q} = \frac{k \frac{\partial T}{\partial n}}{\frac{1}{2} \rho_{\infty} u_{\infty}^3}$$

where n is normal to the surface coordinate. The difference in heat transfer for dipole strengths $B_0=1$ and $B_0=2$ appear smaller than that for either one and $B_0=0$. The stagnation point heat transfer is significantly reduced for the full MFD approach, but not so for low magnetic Reynolds number approach, which is at variance with the analysis of Bush and the simulations of Poggie and Gaitonde. This remains unexplained at present.

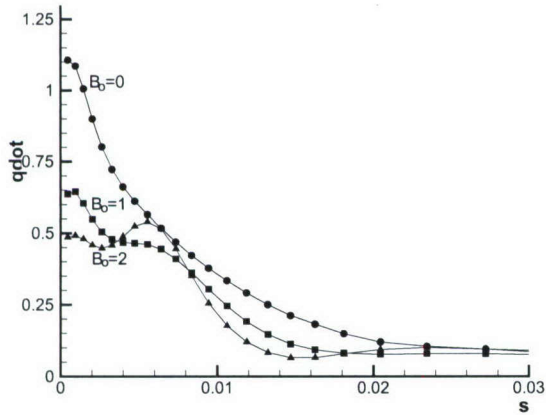


Figure 18 Surface heat transfer, full MFD Eqs.

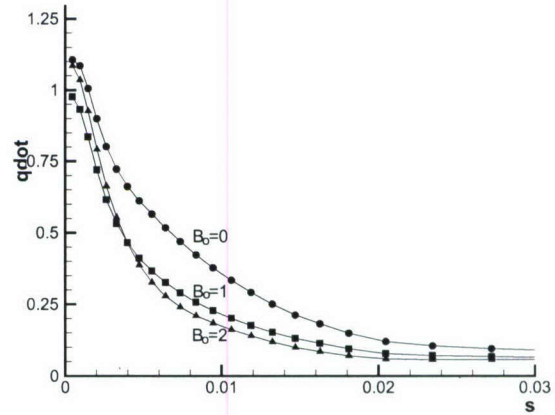


Figure 19 Surface heat transfer, low Re_{mag} Eqs.

Free Stream Effects

It is thought that the effect of the Lorentz force field upon the free stream, ahead of the bow shock wave, may important. The work done on the fluid by these forces plus joule heating could add heat to the free stream, consequently raising its temperature and increasing the speed of sound. This effectively would lower the free stream Mach number, and perhaps explain the increase in standoff distance. The Bush analysis assumed that the electrical conductivity outside the shock layer was zero. Fig.27 compares the flow fields: (1) with the electrical conductivity set to zero ahead of the bow shock wave, top half, and (2) with it defined as before, bottom half. Both used the low magnetic Reynolds number approach with $B_0=2$ Tesla. There is little

difference in the results, as shown in the figure, indicating that the magnetic field's effect on the free stream is not important for this case and Bush's assumption was valid.

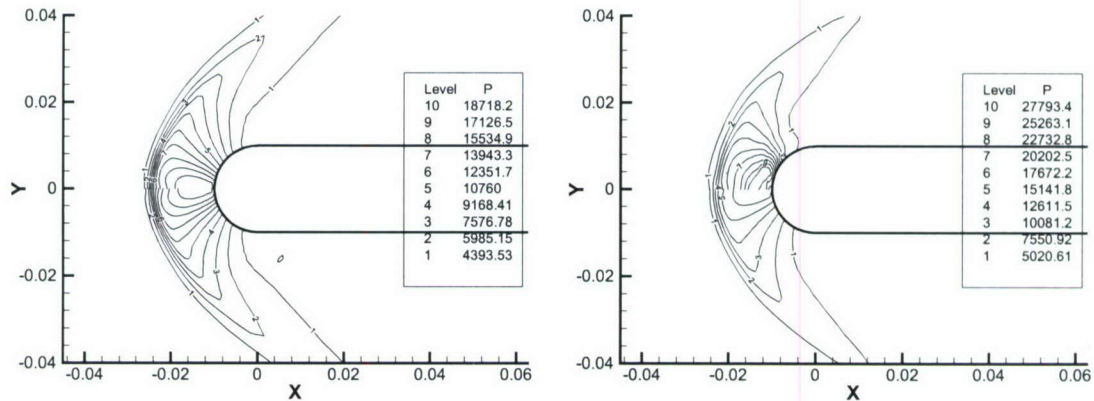


Figure 27 Pressure contours, low Re_{mag} Eqs, **Figure 28** Pressure contours, $B_0=2$, full $B_0=2$, $\sigma_e = 0$ outside shock (bottom half) MFD (top half), low Re_{mag} (bottom half)

Full MFD vs. low Re_{mag}

From the above results and discussion, it can be thought that the difference between the two approaches is solely caused by the differences in the magnetic fields, caused by the addition or not of the induced field to the imposed field. This can be tested by restarting a converged flow simulation using the full MFD approach as the initial condition for a low magnetic Reynolds number simulation. If the above supposition is true, the continued simulation will remain unchanged. Fig.28 shows the pressure contours for both approaches, the converged MFD results on top and the continued solution, using low magnetic Reynolds number approach results, below. Although the shock standoff distance remains the same, the contour patterns are somewhat different. This was not expected and remains unexplained at present.

(2) Internal Flow: Simulation of an “Energy Bypass” Scramjet Engine



Figure 29 Generic Hypersonic Vehicle



Figure 30 Starboard Side Engine Box

Fig.29 shows the surface heating about a generic hypersonic vehicle traveling through the atmosphere at Mach 25. The heating is extreme at the vehicle nose, wing leading edges and engine inlet. MFD may perhaps be used to control the flow in these regions and possibly

alleviate severe heating. It also offers potential to thrust enhancement for proposed scram jet engines. The starboard side engine box of the above vehicle is shown in Fig.30.

To test the new algorithm features discussed herein (the Hall Effect, ion slip and calculation of electrical conductivity via electron and ion number densities), a simplified test geometry was chosen for the engine box. It consists of a rectangular geometry with three sections for MFD power generation, combustion and MFD acceleration, as shown in Fig.31. Each section is 3m long, 5m wide and 1m deep.

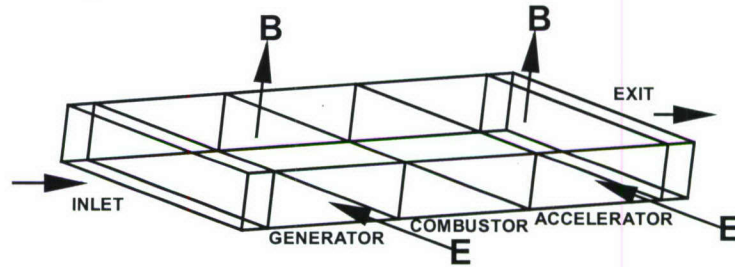


Figure 31 Simplified Scramjet Engine

Magnetic and electric fields are imposed on the flow normal to the flow direction and to each other. The imposed Magnetic field was $B_{y_0} = 1 \text{ Tesla}$ and a local loading factor of 0.75 was used to decelerate the flow in the generator section, from an entering flow of Mach 10 to about 3.5 at the combustor entrance. Heat was added within the combustor at a rate proportional to a fraction of the kinetic energy of the uniform shock-heated free stream, assumed ahead of the inlet, ($u_0 = 6304 \text{ m/s}$, $p_0 = 60 \text{ N/m}^2$ and $T_0 = 1000^\circ \text{K}$). The magnetic field imposed upon the flow within the accelerator was $B_{y_0} = 0.25 \text{ Tesla}$ and the load factor based on free stream velocity was 2.

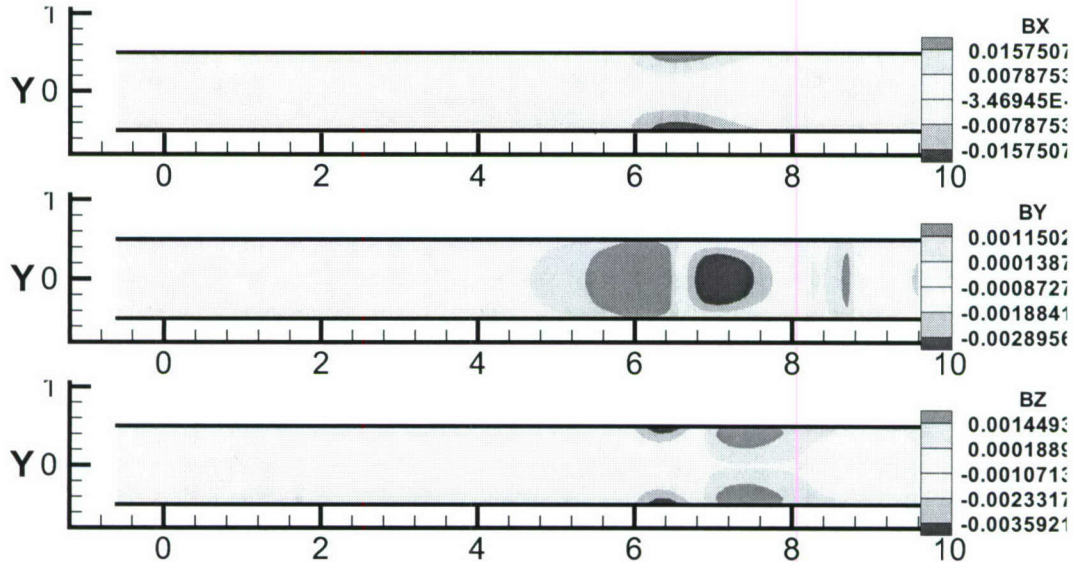


Figure 32 Induced Magnetic Field Components

The induced magnetic field component contours are shown in Fig.32 on an x-y plane at the center of the channel.

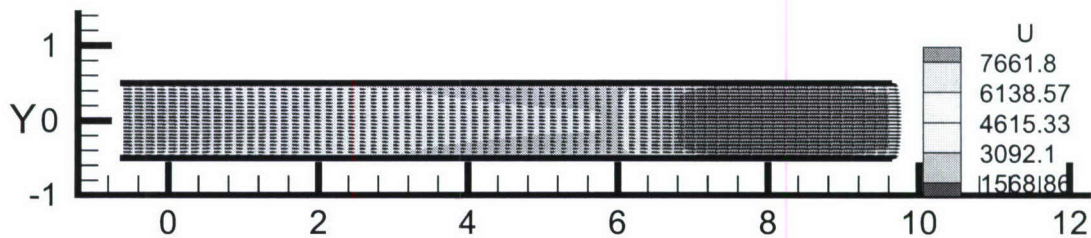


Figure 33 Velocity Vectors and u-Velocity Contours

Velocity vectors and contours of the axial velocity component are shown in Fig.33. The deceleration of the flow within the MFD generator section is shown, followed by further reduction within the combustor and then acceleration within the MFD accelerator section. Contours for electron concentrations and electrical conductivity are shown in Figs. 34 and 35.

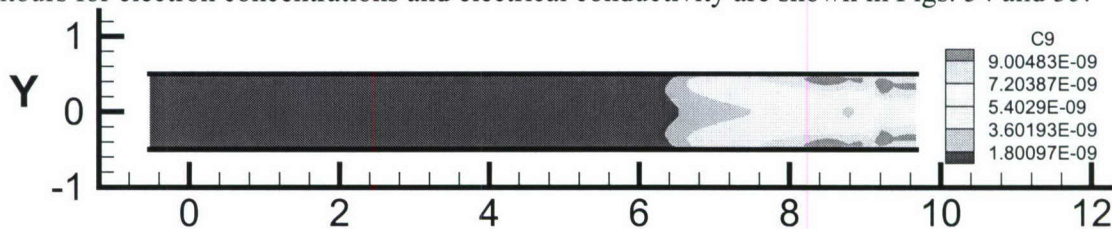


Figure 34 Electron Concentration Contours

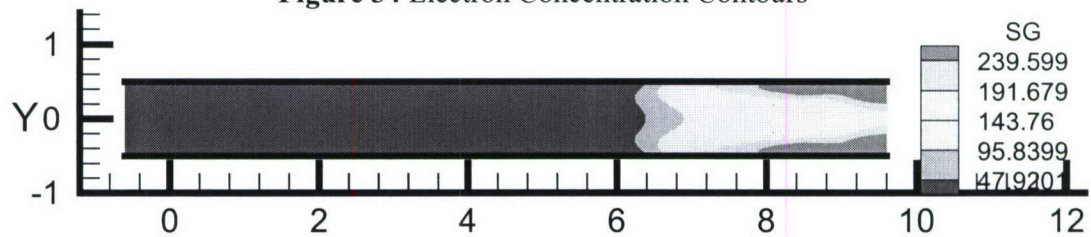


Figure 35 Electrical Conductivity Contours

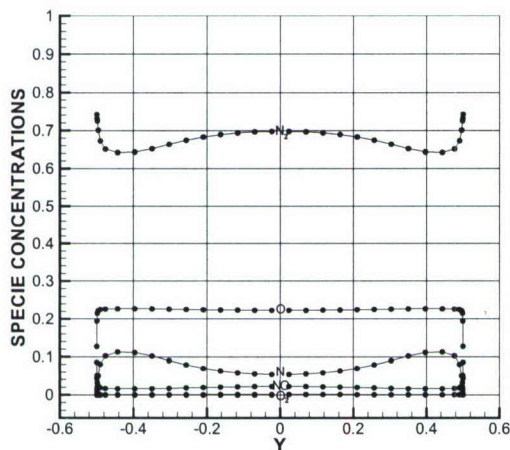


Figure 36 Specie Concentrations

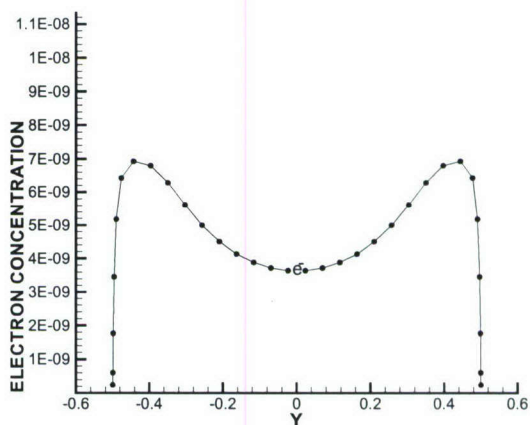


Figure 37 Electron Concentration

Specie concentrations for N_2 , O_2 , NO , N , O and e^- half way through the accelerator section, at $x=7.5m$, are shown in Figs. 36 and 37. Fig.38 shows that both axial thrust and maximum velocity through the channel, normalized by values at the entrance, both decrease with power generation and increase by almost a factor of 50% within the accelerator.

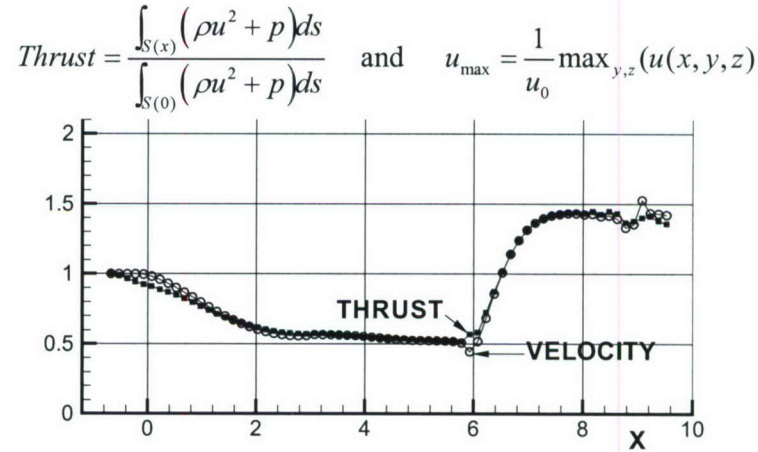


Figure 38 Axial Thrust and Maximum Velocity vs. x

Conclusion

Algorithms have been developed to simulate weakly ionized flows relevant to flow about hypersonic flight vehicles and through energy bypass scram jet engines. These include numerical procedures for casting the governing MFD equations in a form enhancing numerical precision, boundary condition application, scalar and tensor formulations for electrical conductivities for Hall current and ion slip effects, calculation of equilibrium properties for an open ended set component gas species, control of magnetic field divergence and improving the fully implicit algorithm for solving the governing equations. Fairly realistic applications were made test the robustness of the developed procedures.

Although the main thrust of the present study is algorithm development for weakly ionized hypersonic flow simulations within strong magnetic and electric fields, fairly realistic simulations were made of the Ziemer experiment, conducted in the late 1950s. This is a good test problem for algorithm development because of the strong interaction of the magnetic field with the flow and because the gas temperatures are high enough to simulate hypersonic conditions. The present results confirmed earlier studies predicting increased drag and decreased heat transfer with increased magnetic field interaction. They also explain why the low magnetic Reynolds number approach to flow simulation predicts larger bow shock wave standoff distances than the full MFD equation approach, because the induced magnetic field tends to partly cancel the imposed magnetic field. In general the two approaches agree well with one another. Unexplained differences remain between the two approaches that invite further study. The Hall and ion slip effects significantly reduce the interaction of the magnetic and flow fields.

The numerical procedures were applied to simulate the flow through an energy bypass scram jet engine. The gas was assumed to be the chemical equilibrium containing 13 species and 11 chemical reactions. The electron and ion concentrations were used to determine electrical conductivities of seeded air. The algorithm has been applied to a simplified rectangular channel geometry containing sections for MFD power generation, combustion and MFD acceleration. Predictions of engine thrust were calculated.

Acknowledgment/Disclaimer

This work was sponsored (in part) by the Air Force Office of Scientific Research, USAF, under grant/contract number FA9550-04-1-0155. The views and conclusions contained herein are those of the authors and should not be interpreted as necessarily representing the official policies or endorsements, either expressed or implied, of the Air Force Office of Scientific Research or the U.S. Government.

References

- ¹Park, C., Bogdanoff, D. and Mehta, U., 'Theoretical Performance of a Nonequilibrium MHD Bypass Scramjet,' AIAA Paper No. 2001-0792, Jan. 2001.
- ²Mitchner, M., and Kruger, C.H. Jr., *Partially Ionized Gases*, 1973, John Wiley and Sons, Inc.
- ³Park, C., *NonEquilibrium Hypersonic Aerothermodynamics*, 1990, John Wiley and Sons, Inc.
- ⁴*Trnpt* computer program obtained by author from C. Park at NASA Ames Research Center
- ⁵Ziemer, R.W., "Experimental Investigation in Magneto-Aerodynamics," *ARS Journal*, Vol. 29, Sept. 1959, pp. 642, 647.
- ⁶Bush, W. B., "Magnetohydrodynamic-Hypersonic Flow Past a Blunt Body," *Journal of the Aero/Space Sciences*, Vol. 25, Nov. 1958, pp. 685-690.
- ⁷Poggie, J. and Gaitonde, D.V., "Magnetic Control of Flow Past a Blunt Body: Numerical Validation and," *Physics of Fluids*, Vol. 14, No. 5, May 2002, pp., 1720-1731.

Personnel Supported During Duration of Grant

1 PhD and 7 Master Degree Graduate Students, Stanford University

Publications

- MacCormack, R.W., "Flow Calculations with Strong Magnetic Effects," *AIAA Paper No. 2004--0318*, 2004, 42nd Aerospace Science Meeting, Reno NV, January 2004.
- MacCormack, R.W., "Magneto-Aerodynamic Flow Calculations with Strong Magnetic Fields," *AIAA Paper No. 2004--2163*, 2004, 35th Plasmadynamics and Lasers Conference, Portland, OR, June 2004.
- MacCormack, R.W., "Aerodynamic Flow Calculations with Strong Magnetic Induction and Diffusion," AIAA Paper 2005-0559, Jan. 2005.
- MacCormack, R.W., "Evaluation of the Low Magnetic Reynolds Approximation for Aerodynamic Flow Calculations," AIAA Paper 2005-4780, June 2005.
- MacCormack, R.W., "Simulation of Hypersonic Flow with Strong Magnetic Field Interaction," AIAA Paper 2006-0970, January 2006.
- MacCormack, R.W., "Simulation of Hypersonic Flow About an Air Vehicle with Strong Magnetic Field Interaction," AIAA Paper 2006-3232, June 2006
- MacCormack, R.W., "Simulation of Hypersonic Flow with a Strong Magnetic Field," AIAA Paper 2007-0397, January 2007.

MacCormack, R.W., "Numerical Simulation of Aerodynamic Flow within a Strong Magnetic Field with Hall Current and Ion Slip," AIAA Paper 2007-4370, June 2007

Honors & Awards Received

none

AFRL Point of Contact

Dr. Datta Gaitonde, AFRL/VA, WPAFB, OH.

Transitions

Computer code and numerical procedures developed herein are now used by various university researchers sponsored by AFOSR.

New Discoveries

No patents pending